

Formation and composition of organic aerosols from the uptake of glyoxal on natural mineral dust aerosols: a laboratory study

Francesco Battaglia^{1,a}, Paola Formenti¹, Chiara Giorio², Mathieu Cazaunau³, Edouard Pangui³, Antonin Bergé³, Aline Gratien¹, Diana L. Pereira^{1,b}, Thomas Bertin³, Joel F. de Brito⁴, Manolis N. Romanias⁴, Vincent Michoud¹, Clarissa Baldo^{1,3}, Servanne Chevaillier³, Gael Noyalet³, Philippe Decorse⁵, Bénédicte Picquet-Varrault³, and Jean-François Doussin³

¹ Université Paris Cité and Univ Paris Est Créteil, CNRS, LISA, F-75013 Paris, France

² Yusuf Hamied Department of Chemistry, University of Cambridge, Lensfield Road, Cambridge, CB2 1EW, UK

³ Univ Paris Est Créteil and Université Paris Cité, CNRS, LISA, F-94010 Créteil, France

⁴ IMT Nord Europe, Institut Mines-Télécom, Université de Lille, Centre for Energy and Environment, 59000, Lille, France

⁵ Université Paris Cité, CNRS, Itodys, F-75013 Paris, France

^a now at Dipartimento di Scienze Chimiche, Università degli Studi di Padova, Padova, Italy

^b now at [Institute-Institute](#) for Atmospheric and Earth System Research, University of Helsinki, Finland

For submission to Atmos. Chem. Phys.

Corresponding author: P. Formenti (paola.formenti@lisa.ipsl.fr)

Abstract

The uptake of glyoxal on realistic submicron mineral dust aerosol particles from a natural soil (Gobi Desert) is investigated during experiments in a large simulation chamber, under variable experimental conditions of relative humidity (RH), irradiation, and ozone concentrations. The uptake of glyoxal on the dust particles starts as soon as the glyoxal is injected into the chamber. At 80% RH, the measured uptake coefficient of glyoxal on mineral dust is $\gamma = (9 \pm 5) \times 10^{-3}$. The totality of the mass of reacting glyoxal is transformed into organic matter on the surface of the dust particles. The uptake of glyoxal is accompanied by the appearance of marker peaks in the organic mass spectra and a persistent growth in the volume concentration of the dust particles. While the mass of the organic matter on the dust rapidly reverts to values prior to uptake, the organic composition of the dust is modified irreversibly. Glycolic and other organic acids, but also oligomers, are detected on the dust. At 80% RH, compounds ranging from C₄ to C₁₀ are observed as oligomerization products of glyoxal mono- and di-hydrate forms. The study suggests that dust aerosols could play a very substantial role in the formation of organic aerosols at high RH, but also that the

reaction could have potentially important implications for the dust optical and hygroscopic properties, including their pH.

1. Introduction

Mineral dust originates naturally from the wind erosion of arid or semi-arid soils, resulting in the suspension of particles with diameters from fractions to hundreds of microns, which can be transported over thousands of kilometres whilst in the atmosphere (Adebiyi et al., 2023; Mahowald et al., 2014). The total global mass of mineral dust particles emitted annually in the atmosphere is of the order of 4600 Tg yr⁻¹, accounting for approximately 40% of the total annual aerosol emissions (Knippertz and Stuut, 2014; Kok et al., 2021). Major natural source areas of mineral dust are North Africa (~50% of the global annual dust emissions), Asia (~40%), North America, and the Southern Hemisphere (~10%; Kok et al., 2023). Anthropogenic emissions are associated with soil erosion for agriculture, pasture, and deforestation (Tegen and Fung, 1995; Webb and Pierre, 2018), but their contribution to the total annual dust mass loading is uncertain, ranging from 5 to 60% (Chen et al., 2023). Mineral dust significantly impacts the Earth's energy balance by absorbing and scattering radiation in the solar and terrestrial spectra (Di Biagio et al., 2019; Kok et al., 2023) and by influencing the lifetime and optical properties of mixed-phase and ice clouds (e.g., Atkinson et al., 2013; Harrison et al., 2001; Steinke et al., 2016). Current estimates of the effective radiative forcing (sum of direct and indirect) of natural mineral dust are in the range of $-0.07 \pm 0.18 \text{ W m}^{-2}$ (Kok et al., 2023), owing to large uncertainties in the atmospheric mass loading and properties of dust at emission and during transport (Castellanos et al., 2024; Li et al., 2021).

Gas-particle interactions along the dust lifecycle contribute to these uncertainties. Numerous laboratory and field studies show that mineral dust is capable to adsorb various reactive gaseous compounds, which may modify its chemical composition, and in turn to alter optical properties, hygroscopicity and ice nucleation activity but also may affect the oxidative capacity of the atmosphere (Bauer et al., 2007; Chirizzi, 2017; Crowley et al., 2010; Joshi et al., 2017; Liu et al., 2013; Ooki and Uematsu, 2005; Romanias et al., 2012; Seisel et al., 2004; Tang et al., 2017; Turpin and Huntzicker, 1995; Usher et al., 2003; Wagner et al., 2008). Dust aerosol may promote photocatalytic reactions of inorganic gases such as SO₂ and NO₂, initiating nucleation events (Dupart et al., 2012; Nie et al., 2014).

The uptake of volatile organic compounds (VOCs) on mineral dust, such as limonene, toluene (Romanías et al., 2016), isoprene (Zeineddine et al., 2017), phenol (Hettiarachchi and Grassian, 2024), and dicarboxylic acids (Ponczek et al., 2019), is also documented. These reactions may alter the VOC budget in the atmosphere and lead to the formation of secondary organic aerosols (SOA) (Li et al., 2019; Tang et al., 2017; Usher et al., 2003; Xu et al., 2023; Zeineddine et al., 2023), one of the key players of atmospheric chemistry (Shrivastava et al., 2017).

Glyoxal (CHOCHO) is one of the most abundant VOCs in the troposphere (Lewis et al., 2020). It is produced through the oxidation of aromatic compounds like benzene, toluene, and p-xylene (Volkamer et al., 2001) as well as by the photochemical oxidation of isoprene (Chan et al., 2017). The global atmospheric concentrations of glyoxal have been evaluated in the range of 10 – 100 pptv by Fu et al. (2008). However, case studies show sometimes higher concentrations. During a field study in Shanghai in the summer of 2018, Guo et al. (2021) reported an average glyoxal concentration of 164 ± 73 pptv, due to daytime photochemistry. Local concentrations of up to 400 pptv have been documented in regions influenced by aromatic pollution (Li et al., 2022). Satellite measurements of glyoxal show that the highest concentrations in tropical and subtropical regions are found during warm, dry periods influenced by biogenic emissions and vegetation fires, but also anthropogenic pollution (Vrekoussis et al., 2009). Elevated glyoxal concentrations have been observed in aged biomass burning plumes and tropical ocean regions, revealing model under-predictions in high-emission areas due to missing complex organic compound sources (Kluge et al., 2023). Field measurements in the northeast Atlantic Ocean reveal that models generally underestimate glyoxal concentrations due to missing contributions from acetaldehyde and other chemical precursors, and a potential glyoxal source from the ocean surface organic microlayer, particularly significant at night (Walker et al., 2022).

Glyoxal is a very soluble molecule which readily oligomerises in water, leading to the formation of larger molecules (Kalberer et al., 2004; Shapiro et al., 2009). Several previous studies have revealed that glyoxal ~~can~~has the ability to be uptaken up onto aerosol particles, potentially serving as a significant source of organic aerosols (e.g., Liggio et al., 2005b; Carlton et al., 2007; Ervens and Volkamer, 2010; Galloway et al., 2009; Knote et al., 2014). The uptake of glyoxal on ammonium sulphate particles can lead to the formation of carbon-nitrogen compounds (such as imidazole derivatives),

oligomers, and organic acids (Galloway et al., 2009), that has been observed to cause browning (De Haan et al., 2020). The light-absorbing imidazole derivatives formed by glyoxal have been found to act as a photosensitizer, initiating radical chemistry under realistic irradiation conditions in the aerosol phase and initiating aerosol growth in the presence of limonene (Rossignol et al., 2014).

The study by Shen et al. (2016) revealed that glyoxal can also uptake onto synthetic minerals proxies of natural mineral dust, forming oligomers, organo-sulphates, formic acid, and glycolic acid, henceforth suggesting a potential significant mechanism for organic aerosol formation and modification of the optical and hygroscopic properties of mineral dust. Recently, Zogka et al. (2024) highlighted the dependence of the soil composition and size for the uptake of glyoxal on soils and soil surrogates (synthetic mineral).

Following up from those studies, in this paper we present novel laboratory experiments using a large-scale simulation chamber to investigate the formation of organic aerosol from the uptake of glyoxal on realistic airborne mineral dust particles, in atmospherically-relevant conditions. Dust aerosols are generated from a natural parent soil from the Gobi Desert, one of the most important sources of tropospheric dust and representative of an area where this interaction could take place (Wang et al., 2015).

This paper has two major objectives. First, it provides experimental observations of the uptake of glyoxal on mineral dust aerosol, leading to the formation of organic aerosol mass upon interaction and measuring glyoxal uptake coefficient of mineral dust. Secondly, it presents the chemical composition of the mixed organic-dust aerosols, in terms of ~~its~~-their oxidation state, molecular composition and the evolution of SOA content from glyoxal.

2. Experiments and methods

This study uses the CESAM atmospheric simulation chamber (CESAM – Chambre de Simulation Atmosphérique Multiphasique, which translates to Experimental Multiphase Atmospheric Simulation Chamber in English), a 4.2 m³ cylindrical stainless-steel reactor initially described by Wang et al. (2011). CESAM was specifically designed to study multiphase processes involving aerosol particles, gas-phase compounds and water, both in the vapour and liquid phases (Brégonzio-Rozier et al., 2016; Denjean et al., 2014; Giorio et al., 2017). CESAM is equipped with three

140 6.5 kW high-pressure arc xenon lamps (model EX-170GM3-E, IREM SpA, Borgone,
141 Italy) and 6 mm Pyrex plate filters to mimic the solar radiation. A 50 cm stainless-steel
142 four-blade fan located at the bottom of the chamber ensures a mixing time of about 1
143 minute for the gas phase and the homogeneity of the internal composition.

144 2.1. Injection and cleaning protocols

145 Dust aerosols were generated and injected into the chamber according to the protocol
146 detailed in Battaglia et al. (2025) using a natural soil sample from the Gobi Desert
147 (107.48°N; 36.49°E). Prior to use, the soil was sieved at 1000 µm and dried at 100°C
148 for less than ~~one~~ hour to remove adsorbed water and contamination from volatile
149 gases. A quantity ranging from 30 and 50 g was placed in a 1 L Büchner flask and
150 shaken at 100 Hz using a sieve shaker (Retsch® AS200) to simulate the saltation and
151 sandblasting mechanisms through which wind erosion generates airborne dust in the
152 real atmosphere (Di Biagio et al., 2017). An Aerodynamic Aerosol Classifier (AAC,
153 Cambustion®) was placed between the dust generator and the chamber to inject mono-
154 modal dust centred between 300 and 400 nm in geometric diameter.

155 Glyoxal was prepared by heating a mixture of equal amounts of its trimer hydrate
156 (Fluka® Analytical) and P₂O₅ (Sigma – Aldrich ReagentPlus®, 99%) at 150°C (Horowitz
157 et al., 2001). The trimer decomposition occurs inside a vial connected to a vacuum gas
158 manifold. Glyoxal was collected as yellow crystals in a second vial immersed in an
159 ethanol – liquid nitrogen cold trap at around -90°C and then vaporised in a 2.1 L glass
160 bulb to a controlled pressure. This vial was connected to the simulation chamber to
161 inject the glyoxal through a pure nitrogen flow.

162 Ozone was generated by a Corona discharge in pure O₂ using a commercial dielectric
163 ozone generator (MBT 802N, Messtechnik GmbH, Stahnsdorf, Germany). Water
164 vapour was generated by heating ultrapure water (Milli-Q IQ 7000, Merk™) inside a
165 pressurised stainless-steel vessel, previously rinsed at least three times. The total
166 organic carbon (TOC) content of the ultrapure water was monitored to evaluate the
167 influence on the production of organic particles, which was found to be minor (see **Text**
168 **S1 and Figures S1 and S2** in the Supplementary Material). The relative humidity (RH)
169 inside the chamber was measured by a HMP234 Vaisala® humidity and temperature
170 transmitter. Before each experiment, the chamber was evacuated down to 10⁻⁴ mbar
171 and then filled with a mixture of 80% N₂ (Messer, purity > 99.995%) and 20% O₂ (Linde

Mis en forme : Police :Gras

5.0, purity 99.999%) to an internal pressure exceeding by about 5 to 10 mbar the room atmospheric pressure, to prevent accidental contamination during the experiments.

2.2. Instrumentation

The CESAM chamber was equipped with a suite of standard instrumentation for the detection of the aerosol and the gas-phase, whose details are reported in **Table S1**.

Gas-phase glyoxal was measured by a combination of in-situ long-path Fourier Transform Infra-Red (FTIR) spectrometry (Bruker Tensor 37) in the 2720-2930 cm^{-1} absorption band corresponding to the C–H bonds, by a Cavity Attenuated Phase Shift (CAPS) NO_2 analyser (Model T500U, from Teledyne API) and a Proton Transfer Reaction-Time Of Flight-Mass Spectrometer (PTR-ToF-MS) (KORE Technology®, second generation) operated in H_3O^+ ionization mode for VOC detection. The FTIR spectrometer ~~also provided~~~~provided also with~~ the concentrations of formic acid (HCOOH), measured in the C–O bond vibration band centred at 1105 cm^{-1} ; ozone (O_3), measured in the asymmetric stretching of the absorption band centred at about 1043 cm^{-1} ; and carbon monoxide (CO), detected at about 2143 cm^{-1} . The standard infrared absorption spectra of the compounds used for quantification, along with the specific absorption bands integrated for their quantification, are shown in **Figure S4S3**. CO and carbon dioxide (CO_2) were additionally measured by an APEE ProCeas® analyser. Nitrogen oxides (NO_x) were monitored by ~~the~~ APNA-370 analyser by Horiba®.

The aerosol total number concentration above 2.5 nm was measured by a Condensation Particle Counter (TSI® model 3075). The aerosol number size distribution in the submicron fraction was measured by a combination of a Scanning Mobility Particle Sizer (SMPS) consisting of a Differential Mobility Analyser (TSI®, model 3080) coupled with a Condensation Particle Counter (TSI® model 3072) and an Optical Particle Counter (sky-GRIMM® OPC model 1.109).

The aerosol chemical composition was measured by a combination of online and offline methods. A Time-of-flight Aerosol Chemical Speciation Monitor (ToF-ACSM, Aerodyne Research Inc.) equipped with a standard vaporiser provided quantitative unitary mass resolution spectra between 40 nm and 1 μm vacuum aerodynamic diameter (Fröhlich et al., 2013). The instrument was operated through a Nafion membrane dryer (model PD-50T-12). The organic mass concentration (m_{org}) was

obtained considering a unitary collection efficiency ($CE = 1$) and a relative ionization efficiency (~~REIRIE~~) of 1.4 (Nault et al., 2023).

The glyoxal fragment CH_2O^+ at m/z 30 has an isobaric interference with the NO^+ fragment from nitrate. Following Galloway et al. (2009), the contribution of nitrate to the total signal at m/z 30 was calculated as 1.7 times the intensity of the nitrate signal at m/z 46, which corresponds to the 30/46 signal ratio measured during nitrate calibration. The contribution to m/z 30 of glyoxal was then calculated from the total signal by subtracting the contribution of the nitrate and the contribution of air. The elemental ratios of the organic fraction O/C and H/C are calculated from the measured f_{44} and f_{43} , respectively, following the parametrizations proposed by Aiken et al. (2008) and Ng et al. (2011), respectively.

Filter samples were collected on PTFE filters (Zefluor, 47 mm diameter, 2 μm pore size, Pall Life Sciences) and quartz fiber membranes (Tissuquartz 2500 QATUP, 47 mm diameter, Pall Life Sciences) using a series of custom-made stainless-steel holder of 6-mm diameter operated at 10 L min^{-1} , and preceded by an denuder filled with active charcoal paper to remove ozone and VOCs. The sampling time ranged from 30 minutes to 3 hours. The filter holders and PTFE filters were pre-cleaned with dichloromethane (99.8 %, HPLC grade) in an ultrasonic bath, while the quartz filters were pyrolyzed at 550°C for approximately 8 hours. After sampling, filters were folded and placed in an aluminium paper envelope previously pyrolyzed (same protocol ~~asthan~~ the filters), and stored in a refrigerator at -18°C. Chamber blanks were collected by sampling for about 20 min from the chamber only filled with N_2 and O_2 . Analytical blanks were also collected.

2.3. Filter analysis

The analysis of the filter samples was conducted by a combination of three techniques to provide ~~with-a~~ comprehensive view of the chemical composition of the organic fraction formed on the dust particles as the result of the processing by glyoxal. The full details of the analysers and analytical protocols are reported in as detailed in **Text S2** in the supplementary material. Those include

- 1/ the Supercritical fluid extraction coupled with gas chromatography mass spectrometry (SFE/GC-MS; Chiappini et al. (2006)) for target analysis of low-weight mass fragments derived from molecules linked to glyoxal reactivity (see

Mis en forme : Non Exposant/ Indice

Table S2.1 in the Supplementary Material). such as the m/z 131 fragment (Glyoxylic acid TMS derivatized – CH₃), and the m/z 205 fragment (Glyoxal monohydrate – CH₃);

2/ Electrospray ionization (ESI) high-resolution mass spectrometry (Kourtchev et al., 2015) was used to obtain high-resolution mass spectra and formulae assignments for low-volatility compounds in the ranges m/z 50–500 and m/z 150–1000 (Zielinski et al., 2018). These were processed to provide ~~with~~ parameters describing the carbon oxidation, through O/C and H/C bulk ratios, and the identification of molecular groups such as CHO, CHON, CHOS, CHNS, and CHONS. ESI-HR-MS was also used for a screening- analysis of molecules resulting from the glyoxal transformation due to hydration, oxidation, and oligomerization. These included formulas for mono- and dihydration products (C₂H₄O₃ and C₂H₆O₄, respectively), oxidation products (formic acid (CH₂O₂), glycolic acid (C₂H₄O₃), glyoxylic acid (C₂H₂O₃), and oxalic acid (C₂H₂O₄)), and oligomers formed by the hydrolysis of hydrated glyoxal formulas (linear oligomers with generic stoichiometric formula C_{2n+2m}H_{4n+6m-2(n+m-1)}O_{3n+4m-(n+m-1)}, and ring oligomers with generic formulae C_{2n+2m}H_{4n+6m-2(n+m)}O_{3n+4m-(n+m)}).

3/ X-ray photoelectron spectrometry (XPS) was used following ~~Denjean et al.~~ (2015) to quantify the elemental O/C ratio of the particle surface (O/C_{surf}) to a depth ~~of~~ less than 10 nm. The O/C_{surf} was calculated ~~as~~, as explained in Text S2 in the Supplementary Material. The XPS measurement on a filter collected during one ageing experiment ~~are~~ is shown as an example in **Figure S2.14** in the Supplementary Material.

2.4. Calculation of the aerosol size distribution

The procedure for combining the measurements of the SMPS and the sky-GRIMM® OPC is based on Baldo et al. (2023) and ~~it is~~ described in detail in Battaglia et al. (2025). The number size distributions, expressed in dN/dlogD (cm⁻³), are used to evaluate the total particle surface S (μm² cm⁻³) and volume V (μm³ cm⁻³) by assuming spherical particles as

$$S = \int \pi D^2 \frac{dN}{d\log D} d\log D \quad (2)$$

$$V = \int \frac{\pi}{6} D^3 \frac{dN}{d\log D} d\log D \quad (3)$$

2.5. Calculation of the glyoxal uptake coefficient and rate of particle formation

The uptake coefficient (γ) is defined as the probability of the gas to be taken up on the aerosol surface. It is a unit-less parameter expressed by the ratio between the number of molecules taken up on a surface and the total number of collisions of the gas on the surface as

$$\gamma = \frac{\text{number of total molecules taken up}}{\text{total number of collisions}} \quad (4)$$

The gas-phase uptake coefficient (γ) was estimated from the first-order heterogeneous loss rate of glyoxal (k_{het} , s⁻¹) as

$$\gamma = \frac{k_{het}}{\omega} \quad (5)$$

The rate of collisions (collision frequency, ω) is ~~the~~ defined as

$$\omega = \frac{cA_s}{4} \quad (6)$$

where:

- $c = 146 \times \sqrt{\frac{T}{MW}}$ is the mean molecular speed (m s⁻¹), where T is the air temperature (here 298 K) and MW the molecular weight of the compound of interest (in the case of glyoxal MW = 58 g mol⁻¹).

- A_s is ~~the~~ total aerosol surface concentration (m² m⁻³).

The total aerosol surface concentration (A_s) is calculated from the aerosol size distribution recorded at the end of the dust injection.

The heterogeneous loss rate of glyoxal (k_{het}) due to its uptake on dust particles can be determined as the difference ~~between~~ the loss rate of glyoxal measured during the uptake experiments (k_{obs}) and the glyoxal loss rate on the chamber walls (k_{loss}) as

$$k_{het} = k_{obs} - k_{loss} \quad (7)$$

The glyoxal wall loss is represented by a partition equilibrium described by two first-order reactions: one for the adsorption of ~~gas-phase~~gas-phase molecules onto the chamber walls, and one for the reverse process. The rate constants for both processes have been obtained experimentally through control experiments with only glyoxal in the chamber and at different relative humidity conditions, as detailed in **Text S3** and **Figures S5 to S9** in the supplementary material.

If the uptake reaction is of the first rate, k_{het} is henceforth calculated as

$$k_{het} = \frac{\ln\left(\frac{[Gly]_0}{[Gly]_{obs}}\right) - \ln\left(\frac{[Gly]_0}{[Gly]_{loss}}\right)}{t} \quad (8)$$

where $[Gly]_0$ is the initial concentration of glyoxal, $[Gly]_{obs}$ represents the observed evolution of glyoxal concentration in time, resulting from the sum of uptake and wall loss, and $[Gly]_{loss}$ represents the estimated glyoxal concentration resulting from the wall loss.

The rate of formation of the particulate organic matter (POM; k_{F-POM}) due to the uptake of glyoxal on the dust can be calculated as

$$k_{F-POM} = \frac{\ln\left(\frac{[POM]_t}{[POM]_0}\right)}{t} \quad (9)$$

where $[POM]_0$ represents the initial POM concentration in the particle phase, and $[POM]_t$ represents the concentration of the POM formed at a given time.

In the hypothesis that the POM formation is solely due to the uptake of glyoxal, γ can ~~also be~~also evaluated as

$$\gamma = \frac{k_{F-POM}}{\omega} \quad (10)$$

3. Results and discussion

3.1. Overview of experiments

The ageing experiments of monodispersed mineral dust and glyoxal described in this paper are summarised in **Table 1**. All the aerosol data are corrected for dilution, wall loss, and particle loss through the tubing systems as detailed in **Text S4 and Figures S10 and S11** in the Supplementary Material. Gas phase concentrations are corrected for dilution only.

Table 1. Listing and initial conditions of the experiments considered in this study, including experiments with glyoxal only (experiment type GL), ammonium sulphate and glyoxal (AS + GL), dust only (D) and dust with glyoxal (D + GL). The glyoxal and ozone gas phase concentrations correspond to the maximum value measured by FTIR after the respective injections. V_{seed} indicates the maximum volume concentrations of seed particles (either dust or ammonium sulphate) measured after the particle injection. The notation “dark/light” indicates experiments when filter samples were collected both in the dark and with irradiation.

Experiment type	Reagents	Date	Experiment number	RH, %	Light	[O ₃], ppb _v	Temp, K	[GL], ppb _v	V _{seed} , μm ³ cm ⁻³	
Control	GL	29/04/2021	G ₁	< 5	dark	---	292	1130	---	
		11/02/2022	G ₂	77	light	1440	291	627	---	
	AS+GL	21/02/2023	AS ₁	38	dark	---	298	527	50.1	
		23/02/2023a	AS ₂	35	dark	---	298	516	48.3	
		23/02/2023b	AS ₃	32	light	---	298	445	64.8	
		07/09/2023	AS ₄	81	light	---	301	779	304.1	
		08/09/2023	AS ₅	83	light	---	300	430	161.2	
		D	31/01/2022	D ₁	< 5	dark/light	---	292	---	31.5
	03/02/2022		D ₂	75%	dark/light	---	293	---	55.4	
	Uptake	D+GL	04/02/2022	D ₃	< 5	dark/light	---	293	690	35.6
			08/02/2023	D ₄	32	dark	---	294	940	21.5
09/02/2023			D ₅	31	light	---	295	1050	52.7	
10/02/2023			D ₆	35	dark	---	294	809	37.4	
13/02/2023			D ₇	34	light	---	296	850	51.3	
30/04/2021			D ₈	76	light	---	289	759	28.3	
03/05/2021			D ₉	79	light	---	290	607	38.7	
04/05/2021			D ₁₀	81	light	---	290	371	31.5	
05/05/2021			D ₁₁	78	dark	---	291	805	30.1	
06/05/2021			D ₁₂	82	dark	---	292	432	21.1	
08/02/2022			D ₁₃	81	dark/light	1270	293	555	64.0	
09/02/2022			D ₁₄	78	dark/light	1450	293	756	79.8	
10/02/2022			D ₁₅	75	dark/light	---	295	600	68.4	
14/02/2023			D ₁₆	83	dark	---	296	661	35.8	
15/02/2023	D ₁₇	75	light	---	298	444	41.0			

Table 1 also lists the few control experiments using ammonium sulphate as seed particles, described in detail in **Text S5** [and Figures 12 to 14](#) in the Supplementary Material. No POM formation was observed during control experiments with dust or glyoxal only, both dry and humid conditions and with and without irradiation.

3.1.1. Timeline of particle concentration and composition

The ageing experiments lasted up to five hours. For the experiments carried out in wet conditions, the injection of water vapour preceded the injection of dust. The injection of glyoxal (nominal concentration of 1 ppmv) was conducted at least ~~after~~ 30 minutes after the dust to ensure that the dust particles were homogenously distributed in the reactor. Irradiation was started within one hour after the glyoxal uptake onto the particles. ~~In~~~~On~~ a few experiments, ozone was injected before glyoxal to verify the sensitivity of the reactions to the presence of an oxidant.

The typical timelines of the particle concentrations (number and volume) and the non-refractory composition measured in dry conditions and at 30% and 80% relative humidity are shown in **Figure 1**.

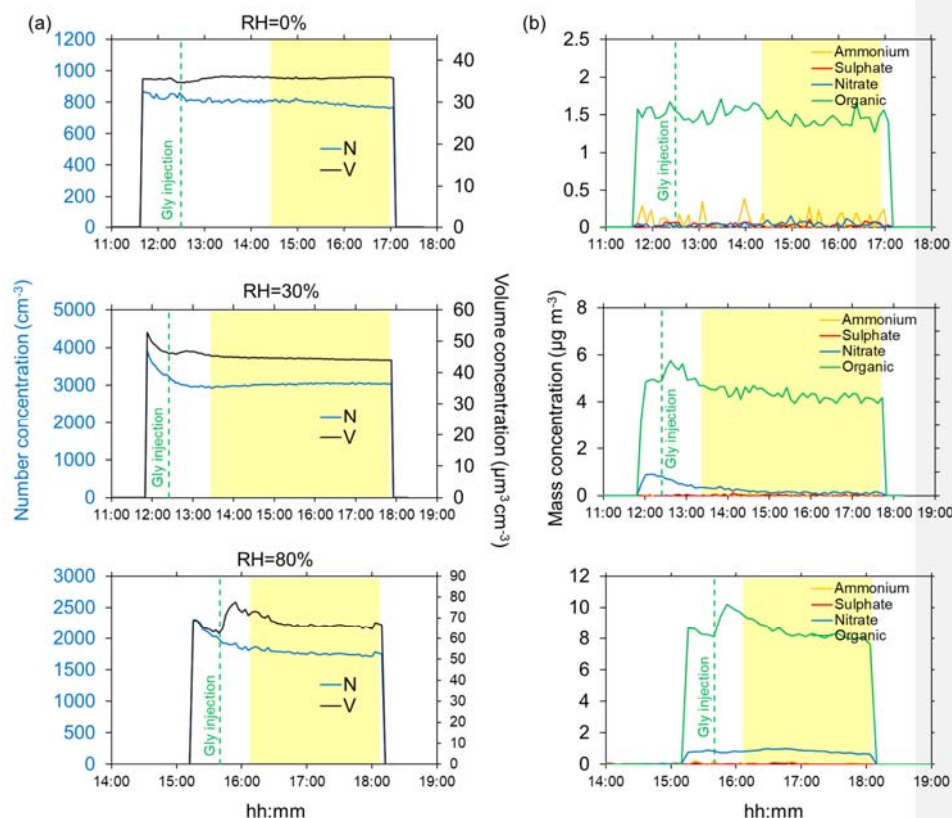


Figure 1. Timeline of ageing experiments of submicron dust with gas-phase glyoxal in dry conditions (top, experiment D₃), 30% (middle, experiment D₇), and 80% RH (bottom, experiment D₁₅). Left (a): aerosol total number (N) and volume (V) concentrations (blue and black lines, respectively) calculated from the measured dust size distributions. Right (b): mass concentrations of ammonium, sulphate, nitrate and organic (yellow, red, blue and green lines, respectively) measured by the ACSM. The yellow-highlighted portion of the graph indicates the interval where irradiation takes place, while the green vertical dashed lines indicate the injection of glyoxal in the chamber. The dust injection corresponds to the time of the initial increase of the number and volume concentrations. Aerosol time series are corrected for dilution, wall loss and particle loss through the tubings.

Figure 1 shows that in dry conditions, there is no significant variation of either the aerosol number or the volume concentrations, nor the chemical composition (including organics) following the glyoxal injection.

At 30% RH, a small increase in the total volume concentration (approximately $5 \mu\text{m}^3 \text{cm}^{-3}$) is observed for about 30 minutes after the injection of glyoxal. This corresponds to an increase of the POM of about $1 \mu\text{g m}^{-3}$, approximately 20% more with respect to

the value measured before the uptake. On the other hand, the particle number concentration shows an apparent decrease at the beginning of the experiments, possibly because the particle loss correction model of Lai and Nazaroff (2000) does not fully apply to dust particles and humid conditions (see discussion in Battaglia et al. (2025). After that, and through the duration of the experiment, however, it remains constant, indicating that the increase in the particle volume occurs on the dust particles and not because of new particle formation.

At 80% RH, the increase in both the total volume and the POM concentrations is more pronounced, approximately $10\text{--}15\ \mu\text{m}^3\ \text{cm}^{-3}$ and $2\ \mu\text{g}\ \text{m}^{-3}$, respectively. As for 30% RH, both total particle volume and the POM concentrations return to values observed prior to the injection of glyoxal, within approximately 30 minutes from their maximum values, likely due to evaporation. A similar behaviour is observed in the presence of ozone (Figure S2–S15 in the Supplementary Material). As for 30% RH, the particle number concentration slightly decreases in time at the beginning of the experiment, but then remains constant, again excluding the formation of new particles but rather confirming the formation of organic matter on pre-existing particles. This is also supported by the fact that the rate of increase of POM and particle volume is the same (slope $3.2 \times 10^{-4}\ \text{s}^{-1}$ and $3.2 \times 10^{-4}\ \text{s}^{-1}$, respectively, for POM and total volume), as shown by Figure S3 S16 in the Supplementary Material.

3.1.2. Timeline of gas-phase concentration

Figure 1 also shows that, while sulphate and ammonium are never detected, a background concentration of nitrate up to $1\ \mu\text{g}\ \text{m}^{-3}$ is measured by the ACSM as soon as the dust particles are injected in the presence of water. We attribute it to the heterogeneous interaction between NO_2 and the dust particles (Goodman et al., 1999), as indeed, a background concentration of a few ppb of NO_2 is present in the chamber as a result of the procedure used to reduce the TOC content in the injected water (see Figure S174 in the Supplementary Material). However, since the contribution of nitrate represents at maximum 1% of the injected dust mass and whether it decreases or remains constant throughout the experiment, its contribution to the particle growth and overall ageing of the mineral dust should be negligible.

Figure 2 shows the time series of the gas-phase compounds detected during the same experiment (D₁₅) at 80% RH.

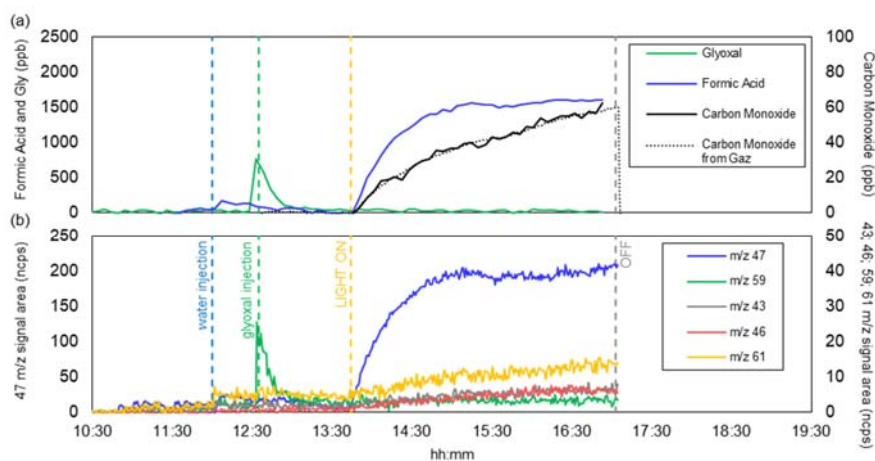


Figure 2. Time series of the gas-phase composition observed during experiment D₁₅: (a) concentrations of carbon monoxide, glyoxal and formic acid measured by FTIR (for CO, the ~~measurements measured~~ of the online analyser are also shown); (b) various VOC ions (m/z 47, 59, 43, 46 and 61) measured by the PTR-MS. Ion signals measured by PTR-MS are normalized by signals of reagent ions (i.e. H₃O⁺ and H₃O⁺(H₂O)) and therefore expressed in normalized counts (ncps). The blue vertical dashed lines indicate the injection of water in the chamber; the green vertical dashed lines indicate the injection of glyoxal in the chamber, the yellow dashed lines indicate the beginning of irradiation, and the grey dashed lines indicate the end of irradiation.

The measured glyoxal concentration after the injection (**Figure 2a**) is lower than the nominal concentration of 1 ppm and goes to zero within minutes due to the rapid interactions with the walls of the chamber, water vapour, and the dust particles. Upon irradiation, formic acid and carbon monoxide are formed, as expected by the photolysis of glyoxal (De Haan et al., 2020). Fragments m/z = 46 and 47 are observed during water injection and photolysis, which could originate from the deprotonated and protonated form of formic acid, respectively. This suggests that a minor fraction of the formic acid could result from the desorption of compounds (including glyoxal) from the chamber walls. Fragments m/z = 43 and m/z = 61, and occasionally m/z = 45 (not seen during experiment D₁₅ and therefore not shown in **Figure 2b**), are observed at a normalised intensity two orders of magnitude lower than that of formic acid, but not attributed. The quantification with both PTR-MS and FTIR in our experimental RH conditions is complex due to water presence, which reduces the sensitivity of PTR-MS and can interfere with the absorption of various organic compounds, making their quantification less accurate.

3.2. Evaluation of glyoxal uptake coefficient and rate of formation of organic aerosols

Figure 3 shows an example of the temporal evolution of the natural logarithm of the glyoxal concentration measured by the FTIR, compared to that measured during a typical blank experiment without dust particles (top panel) and the variation of the aerosol organic fraction measured by the ToF-ACSM during the same time period (lower panel).

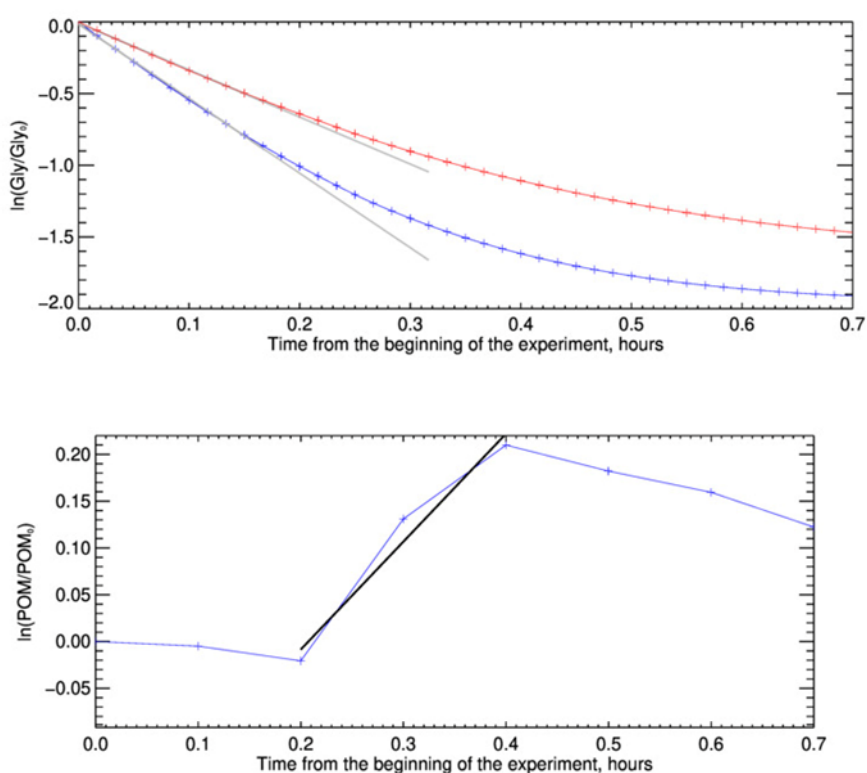


Figure 3. Measurement of glyoxal uptake coefficient on dust for the experiment D₁₅, conducted at 80% RH. The figure compares the two methods for measuring the uptake coefficient. In the top image, results are shown for the method based on monitoring the decay of gas-phase glyoxal. The red and blue curves represent the logarithm of the ratio between the calculated decay of gas-phase glyoxal in the absence and presence of dust aerosols, respectively. The black lines represent the linear fit whose slope provides the heterogeneous kinetic constants of the two processes. The image at the bottom displays the result of the uptake coefficient measurement for the same experiment, obtained from the organic formation on the dust aerosol monitored by the ToF-ACSM. The blue time series shows the logarithm of the ratio between the measured organic concentration divided by the initial organic on dust aerosol, while the black line is the linear fit representing the kinetics of organic formation.

Within the first 10 minutes after the injection of glyoxal, the decrease of the natural logarithm concentrations ratio with time in the presence of dust is linear (that is, the rate is constant). After that, the loss slightly deviates from linearity. The difference from linearity is more evident for the blank experiment, when it occurs earlier than when the dust is present. These observations indicate that, within the first 10 minutes, the uptake of glyoxal on the dust particles can be considered to follow a first-order kinetics and its rate represents an initial uptake coefficient. In the following 20 minutes approximately, the uptake slows down, possibly because all the sites available on the particle surface become occupied, but also because that desorption from the particle surface could reinject glyoxal into the reactive mixture. On the particle phase, the natural logarithm of the organic concentration, normalised by its initial value, increases rapidly and linearly, almost on the same time scale as that of the loss of glyoxal, but then decreases to return to its initial value within approximately one hour. These observations confirm that the uptake of glyoxal results in the formation of OA on the dust particles, but that this process is reversible.

The uptake coefficients calculated as the linear fit of the glyoxal and particle organic concentration are presented in Table 2.

Table 2. Uptake coefficients for glyoxal on mineral dust and ammonium sulphate calculated from the loss of gas-phase glyoxal ($\gamma_{\text{gly-dust-gas}}$) and the rate of OA formation ($\gamma_{\text{gly-dust-gas}}^{\text{OA}}$) for the experiments conducted at 80% RH. The initial glyoxal concentration is reported. The aerosol surface concentration (A_s) corresponds to the value preceding the glyoxal injection. Ozone concentration is the maximum concentration measured by FTIR spectroscopy after the injection. For ammonium sulphate, only the γ values calculated from the loss of gas phase glyoxal are presented, as the ACSM collection efficiency (CE) for ammonium sulphate varies significantly during OA formation (Matthew et al., 2008).

Date	Experiment ID	RH%	[GL] ₀ , ppbv	Ozone (ppb)	A_s (m ² m ⁻³)	ω (s ⁻¹)	$\gamma_{\text{gly-dust-gas}}$	$\gamma_{\text{gly-dust-gas}}^{\text{OA}}$
30/04/2021	D ₈	76	759	---	4.8×10^{-4}	3.9×10^{-2}	6.0×10^{-3}	1.0×10^{-3}
03/05/2021	D ₉	79	607	---	6.1×10^{-4}	5.0×10^{-2}	1.5×10^{-2}	1.5×10^{-2}
04/05/2021	D ₁₀	81	371	---	5.1×10^{-4}	4.2×10^{-2}	1.7×10^{-2}	9.0×10^{-3}
05/05/2021	D ₁₁	78	805	---	4.6×10^{-4}	3.8×10^{-2}	8.0×10^{-3}	5.0×10^{-3}
06/05/2021	D ₁₂	82	432	---	3.5×10^{-4}	2.9×10^{-2}	1.2×10^{-2}	2.3×10^{-2}
08/02/2022	D ₁₃	81	555	1270	7.1×10^{-4}	5.8×10^{-2}	4.0×10^{-3}	4.0×10^{-3}
09/02/2022	D ₁₄	78	756	1450	8.5×10^{-4}	7.0×10^{-2}	4.0×10^{-3}	5.0×10^{-3}
10/02/2022	D ₁₅	75	600	---	8.4×10^{-4}	6.9×10^{-2}	1.0×10^{-2}	5.0×10^{-3}
14/02/2023	D ₁₆	83	661	---	6.0×10^{-4}	4.9×10^{-2}	4.0×10^{-3}	1.5×10^{-2}
07/09/2023	AS ₄	81	779	---	6.3×10^{-3}	5.2×10^{-1}	9.8×10^{-4}	---
08/09/2023	AS ₅	83	430	---	2.0×10^{-3}	1.7×10^{-1}	1.2×10^{-3}	---
Average dust							$9 (\pm 5) \times 10^{-3}$	$9 (\pm 7) \times 10^{-3}$
Average AS							$1.1 (\pm 0.2) \times 10^{-4}$	

Mis en forme : Police :Non Italique

Mis en forme : Police :Non Italique, Non Exposant/Indice

Mis en forme : Police :Non Italique

Mis en forme : Police :Non Italique

Mis en forme : Police :Non Italique, Non Exposant/Indice

Mis en forme : Indice

473

474 The average uptake coefficients for glyoxal on the Gobi mineral dust calculated at 80%
 475 RH from the gas-phase uptake and the particle formation are $\gamma_{\text{Gly-Dust-gas}} = 9 \times 10^{-3}$
 476 (standard deviation ± 5) and $\gamma_{\text{Gly-Dust-OA}} = 9 \times 10^{-3}$ (standard deviation ± 7), respectively.
 477 The two average values agree. This suggests that every glyoxal molecule in the gas
 478 phase is taken up by the airborne dust particles. This ~~also suggests~~suggests also that
 479 the uptake occurs on airborne particles only, as expected, as the dust particles are
 480 selected in the submicron range and that minimal deposition of dust particles is
 481 observed in the first 30 minutes after injection. The primary mechanism of particle loss
 482 during this period is dilution, which does not interfere with uptake. The standard
 483 deviations of the mean values are large, being attributed to the fact that the state of
 484 the chamber walls and the dust size distribution vary from one experiment to the other,
 485 and that the aerosol/chamber walls surface ratio is very low ($0.08\text{-}1.5 \times 10^{-3}$).

486 The presence of ozone appears to be uninfluential. Hanish and Crowley (2003a)
 487 investigated the combined uptake of O₃ and HNO₃ onto dust, and showed that the
 488 uptake of HNO₃ on dust was not influenced by the presence of O₃ (and conversely, the
 489 uptake of O₃ was not influenced by the presence of HNO₃). These authors attributed
 490 these observations to the fact that in their experiments, O₃ concentrations were in
 491 excess by more than three orders of magnitude with respect to those of HNO₃,
 492 compensating for the fact that the uptake coefficients for O₃ is approximately four
 493 orders of magnitude lower than for HNO₃ (Hanish and Croley 2003b; Chang et al.,
 494 2005). In these conditions, which are not generally met in the atmosphere, the
 495 presence of O₃ could result in the modification of surface chemical characteristics, or
 496 to competition for adsorption sites of the two species. These considerations are
 497 applicable to our experiments, as the uptake coefficients of O₃ and glyoxal are of
 498 comparable magnitudes, and we use comparable concentrations.

500 3.3. Evidence of irreversible particle growth

501 **Figure 1** shows that, even in the more favourable conditions (RH=80%), the ratio
 502 between the observed increase of the POM ($2 \mu\text{g m}^{-3}$) and that of the particle volume
 503 concentration ($20 \mu\text{m}^3 \text{cm}^{-3}$) corresponds to an estimated mass density of the order of
 504 0.1 g cm^{-3} , which is about 10 times lower than the value of 1 g cm^{-3} expected for glyoxal.

Mis en forme : Normal, Justifié

Mis en forme : Police :Arial, 12 pt

Mis en forme : Police :12 pt, Couleur de police :
Automatique

Mis en forme : Police :12 pt, Couleur de police :
Automatique

Mis en forme : Police :12 pt, Couleur de police :
Automatique, Indice

Mis en forme : Police :12 pt, Couleur de police :
Automatique

Mis en forme : Couleur de police : Automatique

Mis en forme : Police :12 pt, Couleur de police :
Automatique

Mis en forme : Couleur de police : Automatique

Mis en forme : Police :12 pt, Couleur de police :
Automatique

Mis en forme : Police :12 pt, Couleur de police :
Automatique

Mis en forme : Police :14 pt

Mis en forme : Normal, Justifié

505 This is partially attributed to the fact that only part of the organic matter formed on dust
506 is detected by the ACSM. On the other hand, **Figure S3-S16** shows that, after reaching
507 its maximum value, the volume concentration decreases at a lower rate than the POM
508 (slope $3.9 \times 10^{-5} \text{ s}^{-1}$ and $6.1 \times 10^{-5} \text{ s}^{-1}$, respectively). This suggests that an additional
509 process could contribute to the particle volume concentration, partially compensating
510 for the loss of organic matter on the dust particles.

511 This is confirmed by **Figure 4**, which shows the variation in time of the normalised
512 particle volume distributions, at four steps of the experiments performed at 30% RH
513 and 80% RH. Those include prior and glyoxal injection, POM maximum peak value,
514 and the end of the experiment.

515

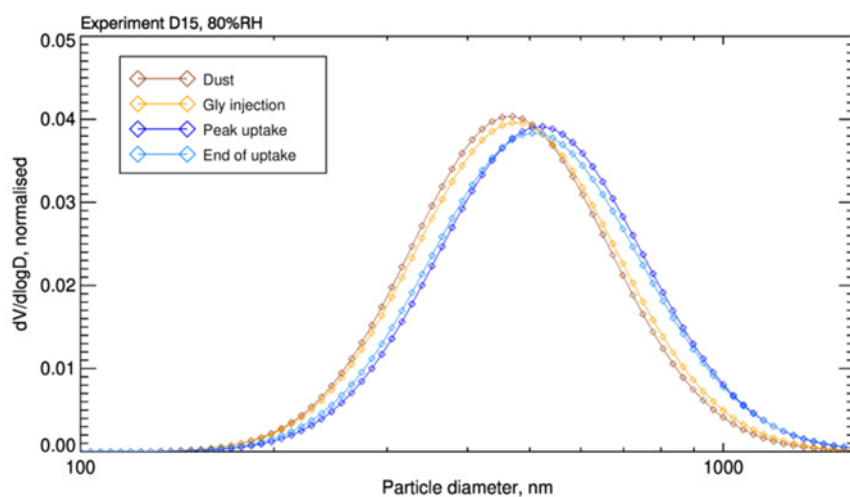
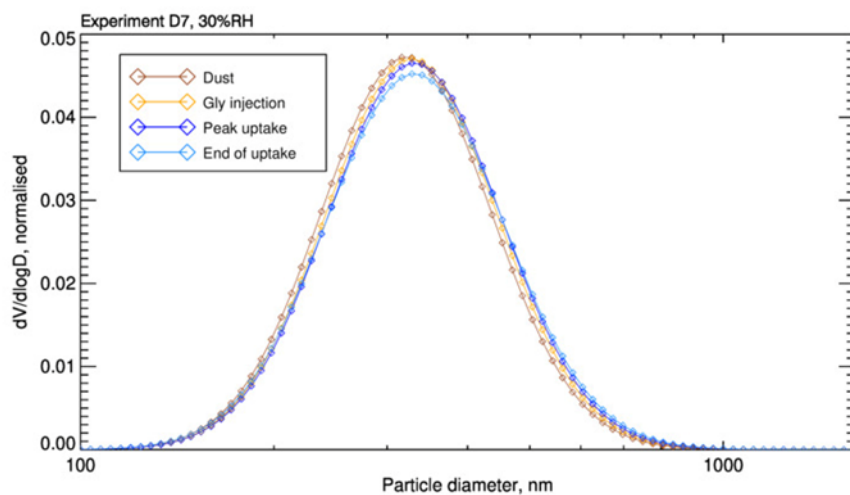


Figure 4. Evolution of volume-size distributions for two glyoxal uptake experiments in different relative humidity conditions. The images illustrate the progression of volume-size distributions recorded at four key moments during the experiments. The first distribution (orange) is recorded after the dust is injected into the simulation chamber. The second distribution (yellow) is recorded at the moment of glyoxal injection. The third distribution (blue) corresponds to the peak uptake of glyoxal on the aerosol, and the fourth (light blue) is recorded at the end of the glyoxal uptake process. The left image depicts the evolution for the experiment D7 conducted at 30% RH, while the image on the right shows the distributions for the experiment D15 conducted at 80% RH. The results highlight that the distributions grow more significantly at 80% RH, indicating a higher glyoxal uptake and organic formation at elevated humidity levels.

All distributions have a single mode. However, after the injection of glyoxal, the geometric mean volume diameter, measured at the maximum POM concentration, increases by up to 10% (from 310 to 340 nm) at 30% RH, and up to 20% (from 450 to 540 nm) at 80% RH. Interestingly, even at the end of the experiment, when the POM concentration returns to its initial value, the increase in geometric mean diameter of the aerosol is irreversible. We hypothesize that the uptake of glyoxal enhances the dust hygroscopicity. Therefore, the difference in total volume between the beginning and end of the experiment is due to formed organic aerosol mass, resulting from water uptake.

3.4. Chemical composition of the particulate organic matter

This section discusses the chemical composition of the particulate organic matter formed on the mineral dust following the interaction with glyoxal. The list and conditions of the filter samples analysed by SFE/GC-MS and ESI-Orbitrap are reported in **Table S2** in the Supplementary Material. Details of the organic composition of the native dust are provided in **Text S6 and Figures S18 to S20**.

3.4.1. Timeline of chemical evolution

Figure 5 shows the time evolution of the intensity of the organic fragments detected by the ToF-ACSM at 80% RH (experiment D₁₅) at four moments of the experiment: 1) before the injection of glyoxal; 2) during the uptake and the formation of the organic matter; 3) after the organic matter has reached its maximum concentration; and 4) at the end of the experiment, when the organic matter returned to its initial concentration.

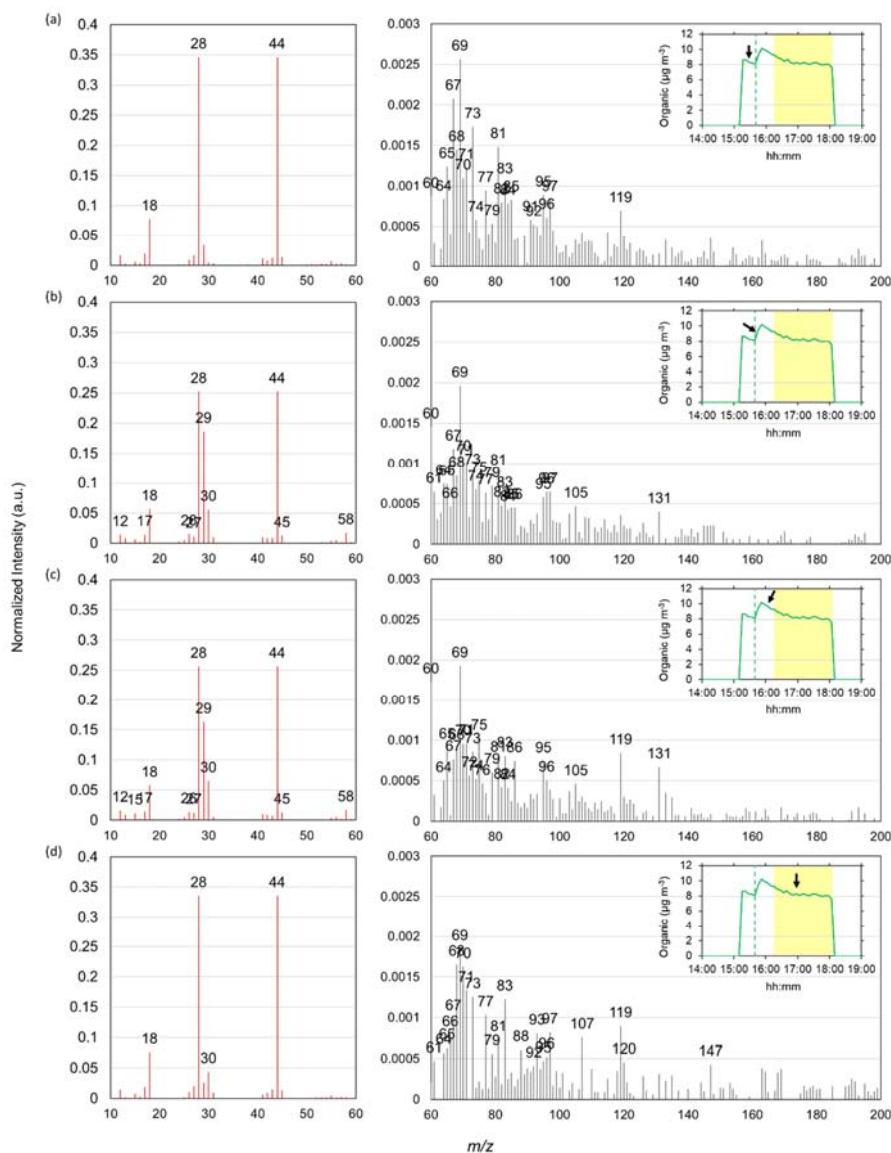


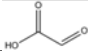
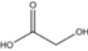
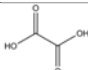
Figure 25. ACSM organic mass spectra (intensities normalized to the total organic concentration) recorded during the experiment D₁₅: (a) before glyoxal uptake (dust organic fraction composition), (b) during glyoxal uptake, (c) after reaching the maximum uptake on the particles and (d) 1h later under irradiation. Panels on the left show the mass spectra ranging from m/z 10 to 60, while the panels on the right represent fragments from m/z 60 to 200 (their intensity is approximately one hundred times lower). The inserts display the time series of organic concentrations measured by the ToF-ACSM. A black arrow indicates the time corresponding to the mass spectrum shown. The yellow-highlighted shaded area indicates the interval where irradiation takes place, while the green vertical dashed lines indicate the moment of glyoxal injection in the chamber.

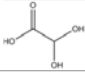
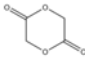
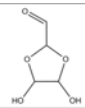
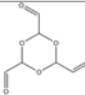
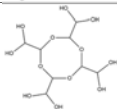
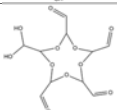
Figure 5 reveals that the organic matter formed as a result of the interaction between mineral dust and glyoxal is composed of oxidized organic fragments, organic acids, and oligomers. Oxidized organic fragments such as CO^+ (m/z 28) and CO_2^+ (m/z 44) are observed through all phases of the experiments. Fragments such as CHO^+ (m/z 29), CH_2O^+ (m/z 30), and $\text{C}_2\text{H}_2\text{O}_2^+$ (m/z 58), appear during the uptake of glyoxal, but diminish over time, due to oligomerization or further oxidation processes. The most intense fragment above m/z 60 is m/z 69, which appears unrelated to glyoxal reactivity but could be attributed to nitrogen-containing organic species such as $\text{C}_3\text{H}_3\text{NO}^+$, originating from glyoxal–ammonia reactions (Galloway et al., 2009) or plant and soil residues (Sun et al., 2010; Nieder et al., 2018). Fragments at m/z 105 and 131, observed consistently during the uptake and the photolysis, could be attributed to condensed glyoxal hydrates (Liggio et al., 2005; Carlton et al., 2007). Fragments at m/z 119 and 120, associated with oxidized products from isoprene-derived aerosols (Safi Shalamzari et al., 2013), increased after glyoxal uptake and under irradiation, suggesting the formation of oxidized oligomers. Upon irradiation, the appearance of m/z 147 and 165 – products of aqueous glyoxal oxidation and oligomer condensation (Lim et al., 2010) – suggests photo-chemically enhanced transformation, though their presence in native dust also points to reversible adsorption processes.

3.4.2. Molecular identification

The list and conditions of the samples analysed by SFE/GC-MS and ESI-Orbitrap are reported in **Text S7** and **Figures S21 and S22** in the Supplementary Material, which also provides with examples of analysis. The summary of the organic molecules detected by those analysis is presented in **Table 3**.

Table 3. Summary of observed compounds identified by SFE/GC-MS analysis and glyoxal-related formulas observed with ESI-Orbitrap, along with the suggested structures under the different experimental conditions tested.

Molecular formula	Name	Tentative Structure	Technique	Experimental conditions
$\text{C}_2\text{H}_2\text{O}_3$	Glyoxylic acid		ESI-Orbitrap	Dust+Gly, 80%, Dark, O_3
$\text{C}_2\text{H}_4\text{O}_3$	Glycolic acid		ESI-Orbitrap SFE/GC-MS	Dust+Gly, 30%, Dark Dust+Gly, 30%, Light Dust+Gly, 80%, Light Dust+Gly, 80%, Light, O_3
$\text{C}_2\text{H}_2\text{O}_4$	Oxalic acid		ESI-Orbitrap	Dust+Gly, 80%, Light

$C_2H_4O_4$	Glyoxylic acid monohydrate		ESI-Orbitrap SFE/GC-MS	Dust+Gly, 80%, Light
$C_4H_4O_4$	Glycolic acid dimer		ESI-Orbitrap	Dust+Gly, 80%, Light
$C_4H_6O_5$	Glyoxal oligomer		ESI-Orbitrap	Dust+Gly, 80%, Light
$C_6H_6O_6$	Glyoxal oligomer		ESI-Orbitrap	Dust+Gly, 80%, Light
$C_8H_{16}O_{12}$	Glyoxal oligomer		ESI-Orbitrap	Dust+Gly, 80%, Light
$C_{10}H_{12}O_{11}$	Glyoxal oligomer		ESI-Orbitrap	Dust+Gly, 80%, Dark

Oxidized organic compounds such as glycolic acid ($C_2H_4O_3$), oxalic acid ($C_2H_2O_4$), and a possible dimer of glycolic acid ($C_4H_4O_4$) were mainly observed under irradiated conditions, while their hydrated forms also appeared in dark conditions. Glyoxylic acid was detected in dark conditions in the presence of ozone. Glycolic and glyoxylic acids consistently form under humid conditions, indicating that their pathways may be less sensitive to water competition or that their precursors interact more strongly with dust surfaces. Light but also ozone tends to favor the formation of glycolic acid from glyoxal at high RH (**Figure S7.1**), suggesting two possible oxidative pathways. Glycolic acid is also detected at 30% RH (not showed), with and without irradiation, in agreement with the experiments on dust by Shen et al. (2016), but differently than reported by Galloway et al. (2009) on ammonium sulphate. Monohydrated glyoxylic acid is found in one sample at 80% RH under irradiated conditions, likely due to the known pattern of oxidation of glyoxal and glycolic acid with OH radicals (Buxton et al., 1997). Unlike previous studies (Galloway et al., 2009; Rubasinghege et al., 2013; Shen et al., 2016), formic acid was not detected on the particle phase despite high concentrations observed in the gas phase (Figure 2), possibly due to high RH suppressing its formation by limiting access to reactive surface sites, as suggested by Shen et al. (2016). It can be hypothesized that formic acid was not detected in the particle phase due to the low amount of organic material on the filter samples and the unsuitability of

Mis en forme : Police :Gras

the method used (due to interferences at the retention time where formic acid is expected).

Oligomerization products (compounds from C4 to C10) of the glyoxal mono- and dihydrate forms, are observed only at 80% RH. These are: C₄H₆O₅ (1 monohydrated glyoxal + 1 dehydrated glyoxal forming a 5-atom ring), C₈H₁₆O₁₂ (4 dehydrated glyoxal molecules forming an 8-membered ring), and C₁₀H₁₂O₁₁ (4 monohydrated glyoxal molecules + 1 dehydrated glyoxal molecule forming a ring structure). The oligomer C₆H₆O₆ (3 molecules of monohydrated glyoxal forming a 6-membered ring) is detected only under dark conditions. C₈H₁₆O₁₂, can correspond to an oligomer previously observed by Shen et al. (2016) on mineral dust.

The persistence of low-volatility, heavy compounds, such as oligomers at the surface of mineral dust has implications for its oxidation state, which is modified in an irreversible way its surface composition, as already shown by previous studies on ammonium sulphate seeds (Kroll et al., 2005; Galloway et al., 2009; De Haan et al., 2020; Hu et al., 2022). This is illustrated by the van Krevelen diagrams obtained from the ESI-Orbitrap analysis in **Figure 6**.

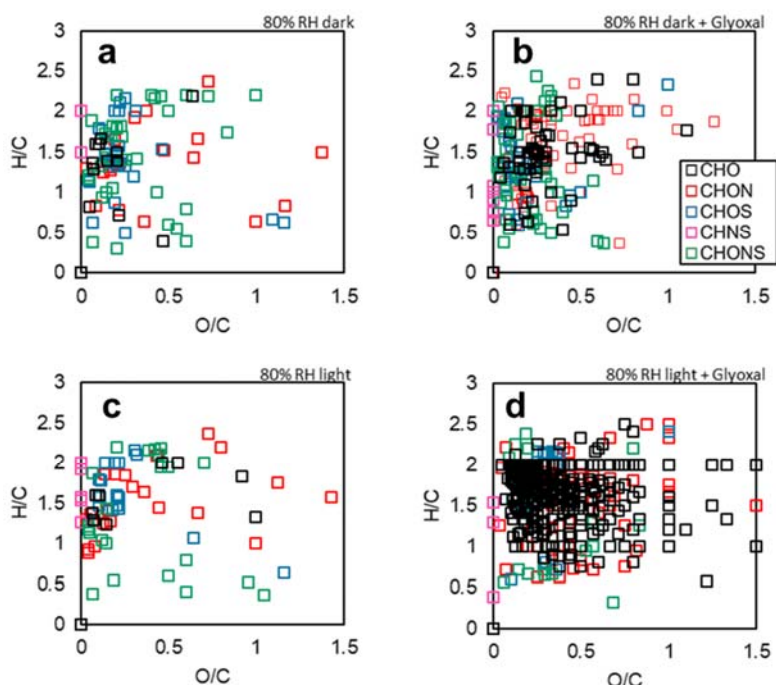


Figure 6. Van Krevelen diagrams recorded at 80% RH for: in the top line experiments in the dark for mineral dust only (control experiment D₂, left) and one ageing experiment of dust with glyoxal (experiment D10); bottom line: same with irradiation. Samples are equivalent in terms of load of particulate organic matter. These are 0.9 µg (sample a), 0.8 µg (sample b), 1.7 µg (sample c) and 0.6 µg (sample d). Despite an equivalent loading of particulate organic mass, the number of signals detected is significantly higher when the dust is exposed to glyoxal (86 and 102 peaks detected for dust only against 398 and 310 with glyoxal, and with and without light, respectively).

The processing by the glyoxal clearly has an effect on the oxidation state of the dust, particularly when lights are on, resulting in the appearance of signals with O/C ratio higher than 1, attributed to photo-oxidation. The predominant family in this case is that of CHO molecules, while the appearance of molecules for families CHON and CHONS is also observed.

4. Discussion

4.1. Comparison of uptake coefficients

The uptake of glyoxal on the dust particles occurs in humid conditions exceeding 30% RH. These observations agree with the results of Liggio et al. (2005a; 2005b) on the uptake of glyoxal on ammonium sulphate aerosols, observing the formation of organic matter only when RH exceeded 50%. Trainic et al. (2011) also observed that the uptake of glyoxal on glycine and ammonium sulphate particles occurred only when the relative humidity was above 35%. On the contrary, both Shen et al. (2016) and Zogka et al. (2024) demonstrated that the uptake can occur in dry conditions too, which was not observed in this work.

At 80% RH, the experimental average of the measured uptake coefficient of glyoxal on mineral dust is $\gamma = (9 \pm 5) \times 10^{-3}$. Our values are approximately one order of magnitude higher than those obtained by Shen et al. (2016), who investigated the uptake of glyoxal on mineral proxies, i.e. SiO_2 , ~~and~~ CaCO_3 and $\alpha\text{-Al}_2\text{O}_3$ under various levels of RH. These authors determined the uptake coefficients after a long exposition of the surface to glyoxal (steady state uptakes) and found that the uptake coefficients decrease with increasing ~~the~~ gas phase concentration of glyoxal. At 1 ppb concentration and 60% RH, the uptake coefficient determined on suspended particles of calcite (CaCO_3) is $1.4 (\pm 0.1) \times 10^{-4}$ and $5.5 \pm (0.1) \times 10^{-5}$ on alumina ($\alpha\text{-Al}_2\text{O}_3\text{AlO}_3$).

Zogka et al. (2024) used a Knudsen cell to evaluate the initial and ~~steady-steady~~ state glyoxal uptake coefficient bulk soil samples of various origins. At low RH, these authors found that for Gobi soil sieved to less than 63 μm in diameter, the initial uptake coefficient using the geometric surface area was 0.18 (corresponding to an upper limit of the uptake), independent of glyoxal concentration. However, the steady state uptake coefficients determined after a long processing of ~~the~~ surface were found to decrease with increasing glyoxal concentration, due to aging of the surface.

Various reasons could induce those apparent differences. First, the differences in the experimental set up as in CESAM, the initial uptake coefficient was measured on dust aerosol particles in suspension in a large volume, compared to sieved soil (Zogka et al., 2024) and grinded mineral powders (Shen et al., 2016). The uptake coefficient is inversely proportional to the available particle surface. In our experiments, the dust available geometric surface density, calculated from the measured size distribution

assuming spherical particles, is in the range $0.35\text{--}6.3 \times 10^{-3} \text{ m}^2 \text{ m}^{-3}$ (**Table 2**). As the ~~the~~ CESAM chamber volume is equal to 4.2 m^3 , the total dust surface area available for the reaction ranges from 2 to $2.6 \times 10^{-3} \text{ m}^2$, several orders of magnitude lower than in the experiments designed by Shen et al. (2016) and Zogka et al. (2024). Shen et al. (2016) used model powders of various sizes between 35 nm and $5 \text{ }\mu\text{m}$, with BET (define BET) surface areas ranging between 1.4 and $440 \text{ m}^2 \text{ g}^{-1}$. In the conservative assumption that only 5 mg of the model powder was used, the total reactive surface area was up to 2.2 m^2 . Zogka et al. (2024) used the soil from Gobi sieved to $63 \text{ }\mu\text{m}$ and a BET surface area of $10.5 \pm 1.0 \text{ m}^2 \text{ g}^{-1}$. Using even just 1 g would yield a surface area of the order of 10.5 m^2 . Differences in the results could also arise by differences in the dust mineralogy, which are difficult to ascertain in the present study.

Our estimated uptake coefficient of glyoxal on mineral dust is also nearly two orders of magnitude higher than for ammonium sulphate ($\gamma_{\text{gas-AS}} = 1.1 (\pm 0.2) \times 10^{-4}$; our study as well as Curry et al., 2018; De Haan et al., 2020; Galloway et al., 2009; Liggio et al., 2005b, a; Trainic et al., 2011), but lower than $\gamma_{\text{gas-AS}} = 2.9 \times 10^{-3}$ at a lower RH (Liggio et al., 2005). The difference could be due to the higher hygroscopicity of ammonium sulphate, enhancing water's competition with glyoxal for adsorption sites at 80% RH, when indeed ammonium sulphate is deliquescent. This suggests, nonetheless, that dust aerosols could play a very substantial role in the formation of organic aerosols at high RH compared to ammonium sulphate, which is often used as an aerosol proxy.

4.2. Mechanism of chemical transformation

Figure 7 illustrates the suggested chemical mechanisms of the transformation of gas-phase glyoxal on the mineral dust particles.

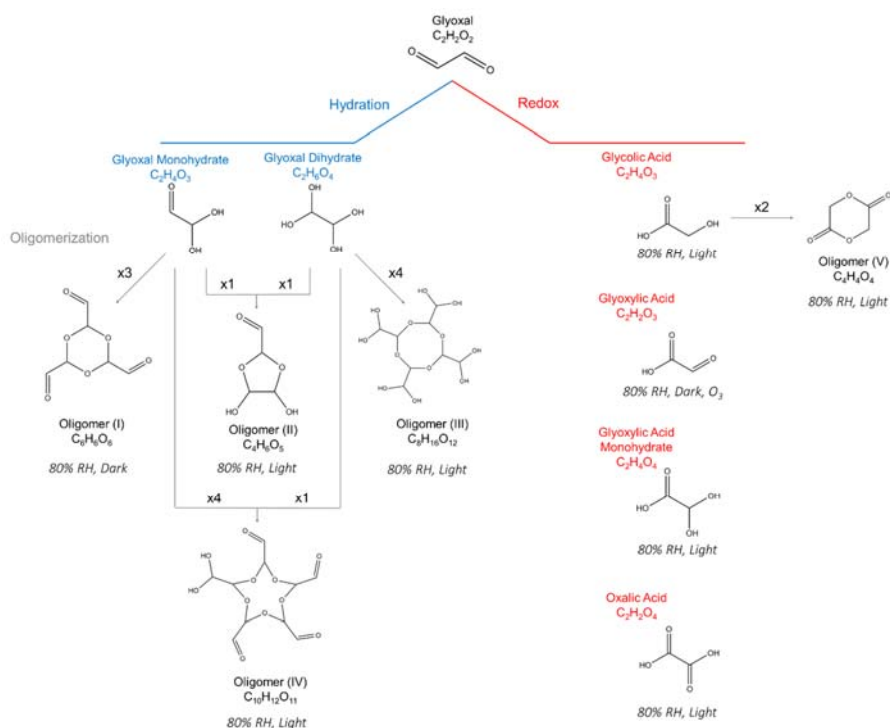


Figure 7. Proposed reaction scheme to explain the glyoxal-related molecular formulas detected through ESI-Orbitrap mass spectrometry and SFE/GC-MS.

The multiphase chemistry of glyoxal on mineral dust particles, leading to the formation of low-volatility, particle-phase products, is complex, involving hydration, redox, and oligomerization pathways. The chemical transformation of glyoxal upon uptake by mineral dust particles primarily occurs through aqueous-phase reactions. The mechanism is initiated by the hydration of glyoxal's aldehyde groups, forming mono- and di-hydrated species. These hydrated intermediates undergo condensation reactions, which involve nucleophilic attack and lead to the formation of cyclic acetal structures, particularly from two to five-membered dioxolane rings. This mechanism is well supported by prior studies (Loeffler et al., 2006; Kua et al., 2008; Hastings et al., 2005), which have described similar pathways for glyoxal oligomerization in aqueous environments.

709 This study provides new insight into ~~how~~-this chemistry on mineral surfaces. While
710 previous research has shown that glyoxal typically forms dimers and trimers in
711 aqueous solution (Liggio et al., 2005; Nozière et al., 2009), our mass spectral data
712 reveal the presence of oligomeric species containing up to 5 glyoxal units. This higher
713 degree of oligomerization - also observed by Shen et al. (2016) - suggests that the
714 particle-phase environment allows for extended oligomer growth. The likely
715 contributing factors include reduced water activity, surface confinement, and enhanced
716 proximity of reactants, all of which promote successive addition reactions that may be
717 hindered in bulk solution (Gomez et al., 2015; Avzianova & Brooks, 2013). Concerning
718 hydration reactions, Shen et al. (2016) showed that both glyoxal and water can
719 accumulate onto dust particle surfaces (as evidenced by FTIR spectra), promoting
720 hydration reactions through surface confinement of the reagents. Absorption of water
721 on dust surfaces can also promote oligomerisation, both directly (hydration is the first
722 step of the oligomerisation reaction) as well as indirectly by enhancing particles' ability
723 to absorb glyoxal.

724 Concerning oxidation, leading to organic acid formation, the dust surface could
725 contribute directly to this mechanism by providing redox reactive sites (Shen et al.,
726 2016). Redox reactions ~~derive-intepromoted the formation of~~ oxidized species such as
727 glycolic, glyoxylic, and oxalic acids. These compounds not only represent aging
728 products but also participate in further condensation reactions, expanding the chemical
729 diversity of SOA. In particular, we detected the presence of oligomer V, which we
730 propose results not from direct glyoxal self-reactions but rather from the condensation
731 of two glycolic acid molecules. This suggests a broader heterogeneous transformation
732 process occurring on the dust surface, possibly involving oxidative pathways. Such
733 cross-reactions are consistent with mechanisms proposed in glyoxal–methylglyoxal
734 systems (Zhang et al., 2022), where mixed oligomers form through shared reaction
735 intermediates.

736 A key aspect of our findings is the irreversibility of glyoxal uptake on mineral dust. In
737 contrast to bulk aqueous systems, where glyoxal oligomerization can exist in
738 equilibrium with monomeric species, our results suggest that oligomer formation on
739 mineral particles is effectively irreversible. The persistence of high-molecular-weight
740 products following drying and thermal analysis confirms that these species are
741 chemically stable and remain in the condensed phase. This behaviour is consistent

with previous observations (Hastings et al., 2005; Ortiz-Montalvo et al., 2014), and highlights the significance of particle-phase reactions in the formation of SOA.

The acidity of the particle surface could potentially play a role in catalysing glyoxal oligomerization. It is plausible that localized acidity arises or is enhanced by the accumulation of transformation products such as glycolic and oxalic acids, which were detected in this study. This in-situ acidification may facilitate acid-catalysed reaction pathways even under neutral or weakly acidic conditions. The importance of acidity in glyoxal chemistry is supported by mechanistic proposals involving carbenium ion intermediates or hydrogen-bond-assisted nucleophilic mechanisms, which can operate effectively without requiring strongly acidic environments (Zhang et al., 2022; Gomez et al., 2015). These pathways are known to promote the formation of low-volatility oligomers, contributing to organic aerosol mass. Similarly, Ortiz-Montalvo et al. (2014) demonstrated that even mildly acidic aerosols significantly enhance glyoxal oligomerization and SOA formation.

Another critical factor is the presence of adsorbed water on mineral dust particles. Our findings demonstrate, in fact, that the availability of surface water facilitates organic aerosol formation from glyoxal. This agrees with chamber and field studies (Hastings et al., 2005; Shen et al., 2016) that identified a RH threshold above which glyoxal uptake dramatically increases. The presence of a thin aqueous film on the particle surface creates a reactive medium where glyoxal can concentrate, hydrate, and polymerize efficiently. Even after evaporation, the products formed are retained in the particle phase, evidencing their low volatility and chemical resilience.

4.3. Implications for the dust properties

The irreversible transformation of the chemical composition of mineral dust following the uptake of glyoxal could influence the physico-chemical properties of mineral dust particles. The formation of organic acids (glycolic, glyoxylic and oxalic acids) should change the dust pH, increasing its acidity and ability to dissolve transition metals like iron and copper. This could alter their speciation, enhancing their bioavailability in aqueous aerosol environments and potentially impacting atmospheric chemistry and the reactivity of aerosol particles (Giorio et al., 2022). Changes in dust pH could also affect its hygroscopic properties, influencing ~~its~~^{their} ability to adsorb water and grow in size. This is consistent with our observation regarding the volume increase of dust particles after the uptake and the subsequent growth that enhances particles.

interaction with light and cloud droplets formation. Collectively, these processes highlight how aerosol acidity modulates not only chemical transformations but also key physical properties and atmospheric lifetimes of dust-glyoxal systems.

The newly formed organic matter from glyoxal on dust particles could also alter the aerosol's optical properties, affecting its ability to absorb solar radiation, as recently observed in aqueous solution (De Haan et al., 2023) or on ammonium sulphate aerosols (De Haan et al. 2020; Trainic et al. 2011). The presence of hydrated glyoxal oligomeric structures has already been observed to have UV radiation absorption properties (Kalberer et al., 2004; Shapiro et al., 2009). Glyoxal-derived oligomers could significantly influence the optical properties of mineral dust aerosols. Spectroscopic analyses revealed that these oligomers have broadened OH and C–O bands and enhanced Raman activity, indicative of their hydrated and cyclic structures (Avzianova and Brooks, 2013). They also have strong UV-visible absorption, particularly between 300–600 nm, with characteristic shoulders at ~280 and 345 nm attributed to acetal and aldol condensation products (Schwier et al., 2010; Shapiro et al., 2009). High RH conditions (> 80%) facilitate brown carbon formation, evidenced by the further appearance of UV-visible absorbance peaks and Raman background signals (De Haan et al., 2020; Zhang et al., 2022).

5. Conclusions

This paper presented a novel investigation of the interaction between gas-phase glyoxal and mineral dust. By taking advantage of the capabilities of the CESAM atmospheric simulation chamber to perform multiphase experiments on time scales relevant to atmospheric processes and dispersion, including aerosols, our experiments considered airborne submicron mineral dust particles generated from a natural soil (Gobi Desert) in realistic concentrations, composition and size distribution. While airborne, the dust aerosol was aged under variable conditions of RH, irradiation, and ozone concentrations. ~~Thanks to the realism of the tools and the experimental conditions,~~ Our study investigates, for the first time, both the rate of uptake of glyoxal and the rate of formation of the organic aerosol from the gas-phase uptake, while providing. ~~We provide~~ the chemical composition of the ~~particle organic matter~~ formed on the dust particles, and ~~their-its~~ implications on the particle microphysics, ~~in atmospheric-relevant conditions.~~

807 This study used a single and instantaneous injection of glyoxal, and not a constant
808 steady state flux. Above 30% RH, upon injection, glyoxal is partitioned almost
809 instantaneously between the gas phase, the chamber walls and the dust particles. This
810 is an advantage to scale our results to ambient conditions. ~~Indeed, Volkamer et al.~~
811 (2005) estimated that the daytime lifetime of glyoxal is around 1.3 h. Alvarado et al.
812 (2020) showed that the long-range transport of glyoxal produced from a point source
813 (e.g., Canadian wildfires) may be possible only by invoking the progressive oxidation
814 of its longer-lived precursors in the plume. In the scenario where dust aerosols interact
815 with a glyoxal plume from a point source, one can expect an interaction time of a few
816 minutes, compatible with that of this study. Furthermore, because the uptake follows a
817 ~~first-order~~ first-order kinetic, the measured uptake coefficient ($\gamma = (9 \pm 5) \times 10^{-3}$
818 at 80% RH) is independent of the glyoxal concentration and transferable to
819 atmospheric conditions.

820 The uptake of glyoxal and the formation of organic matter start as soon as the glyoxal
821 is injected into the chamber and last approximately 20 minutes. After this time, the dust
822 surface seems saturated, likely because of the excessive glyoxal concentrations
823 injected in the chamber. On the other hand, ~~The~~ uptake coefficient measured by the
824 loss of gas-phase glyoxal molecules agrees very well with the rate of formation of the
825 particulate organic mass on the dust, suggesting that the totality of the mass of reacting
826 glyoxal is condensed on the dust particles. While some of the organic matter is lost
827 again from the dust particles due to evaporation, oligomers and organic acids are
828 detected on the dust even after the uptake has finished, indicating that the uptake of
829 glyoxal modifies irreversibly both the composition and the physical properties of
830 mineral dust.

831 This study reveals a significant quantitative transfer of gas-phase glyoxal molecules to
832 mineral dust aerosol surfaces, occurring within a timescale of a few minutes,
833 underscoring the important role of dust-glyoxal interactions in the atmosphere. Our
834 results extend the current understanding of glyoxal chemistry in atmospheric systems.
835 While oligomerization occurs through well-established aqueous-phase pathways, we
836 suggest that mineral dust particles facilitate, in a unique way, higher-order oligomer
837 formation, support irreversible uptake, and possibly promote alternative reaction
838 channels such as glycolic acid condensation. These findings underscore the
839 importance of mineral dust surfaces as active sites for multiphase SOA formation, with

implications for understanding aerosol growth, composition, and climate-relevant properties. This is also in agreement with the field observations conducted by Wang et al. (2015). Neglecting the uptake pathway on dust could result in an underestimation of glyoxal removal from the atmosphere, potentially leading to disparities between model predictions and observed gaseous concentrations of glyoxal (Kluge et al., 2023; Ling et al., 2020; Volkamer et al., 2007; Washenfelder et al., 2011). The findings of this study ~~also have~~~~also~~ important implications for the aerosol direct and indirect radiative effect and aerosol pH. The acidification and the oxidation of the dust aerosols by glyoxal should increase their hygroscopicity, especially under high RH conditions, affecting particle growth dynamics, phase behaviour, and cloud condensation nuclei (CCN) potential (Song and Osada, 2021). Further data analysis ~~are~~~~is~~ ongoing to address these aspects.

Data availability. The simulation chamber experiments that support the findings of this study are available through the Database of Atmospheric Simulation Chamber Studies (DASCS) of the EUROCHAMP Data Centre ([https:// data.eurochamp.org/ data- access/ chamber-experiments/](https://data.eurochamp.org/data-access/chamber-experiments/)).

Code availability. The routine used for fitting the size distribution is available at <https://doi.org/10.5281/zenodo.8135133> (Baldo and Lu, 2023). Note that in this study, we only used the size distribution measured by the OPC instrument, which was fitted with a lognormal function. The ToF-ACSM data processing (including mass calibration, peaks integration and air beam correction of ion intensities) was conducted with Tofware version 3_2_40209, the ACSM data analysis package for the software Igor Pro 7.08 (Wavemetrics, Inc., Portland, OR, USA). SFE-GC-MS data analysis was conducted using the proprietary software (TurboMass Version 6.1.0.1965 PerkinElmer®).

Author contributions. PF, JFD and FB conceptualized the study. PF and FB led the paper writing, with contributions from all the authors. JFD provided with expertise on multi-phase chemistry. CB analysed the aerosol size distribution data. VM supervised the analysis of PTR-MS data. FB, CG and DLP performed the ESI-Orbitrap analysis of filter samples. FB and JFB performed the analysis of ACSM observations. FB, TB and AG performed the SFE/CG-MS analysis of filter samples. FB, GN and SC performed the thermo-optical analysis of filter samples. FB, MC, AB, EP, VM, BPV and PF conducted the chamber experiments. MR provided with the soil sample and expertise on heterogeneous chemistry. PF provided with funding.

Competing interests. The authors declare no competing interests.

Special issue statement. This article is not part of a special issue. It is not associated with a conference.

Acknowledgements. The AERIS data center (www.aeris-data.fr) is acknowledged for distributing and curing the data produced by the CESAM chamber through the hosting of the EUROCHAMP data center (<https://data.eurochamp.org>). The initial contribution of M. Giordano (Afri-SET) to the conceptualisation of the project is gratefully acknowledged. The authors wish to thank the two anonymous referees for helping to improve the manuscript.

Financial support. This work has received funding from the French National Research Agency (ANR) through the research project CLIMDO under the grant number ANR-19-CE01-

884 0008-02. It has received support from the European Union's Horizon 2020 research and
885 innovation program through the EUROCHAMP-2020 Infrastructure Activity under grant
886 agreement no. 730997. CNRS-INSU is gratefully acknowledged for supporting the CESAM
887 chamber as a national facility as part of the French ACTRIS Research Infrastructure. ESI-
888 Orbitrap analyses was supported by a BP next generation fellowship awarded by the Yusuf
889 Hamied Department of Chemistry at the University of Cambridge to CG.

References

- Adebiyi, A., Kok, J. F., Murray, B. J., Ryder, C. L., Stuut, J.-B. W., Kahn, R. A., Knippertz, P., Formenti, P., Mahowald, N. M., Pérez García-Pando, C., Klose, M., Ansmann, A., Samset, B. H., Ito, A., Balkanski, Y., Di Biagio, C., Romanias, M. N., Huang, Y., and Meng, J.: A review of coarse mineral dust in the Earth system, *Aeolian Research*, 60, 100849, <https://doi.org/10.1016/j.aeolia.2022.100849>, 2023.
- Aiken, A. C., DeCarlo, P. F., Kroll, J. H., Worsnop, D. R., Huffman, J. A., Docherty, K. S., Ulbrich, I. M., Mohr, C., Kimmel, J. R., Sueper, D., Sun, Y., Zhang, Q., Trimborn, A., Northway, M., Ziemann, P. J., Canagaratna, M. R., Onasch, T. B., Alfarra, M. R., Prevot, A. S. H., Dommen, J., Duplissy, J., Metzger, A., Baltensperger, U., and Jimenez, J. L.: O/C and OM/OC Ratios of Primary, Secondary, and Ambient Organic Aerosols with High-Resolution Time-of-Flight Aerosol Mass Spectrometry, *Environ. Sci. Technol.*, 42, 4478–4485, <https://doi.org/10.1021/es703009q>, 2008.
- Alvarado, L. M. A., Richter, A., Vrekoussis, M., Hilboll, A., Kalisz Hedegaard, A. B., Schneising, O., and Burrows, J. P.: Unexpected long-range transport of glyoxal and formaldehyde observed from the Copernicus Sentinel-5 Precursor satellite during the 2018 Canadian wildfires, *Atmos. Chem. Phys.*, 20, 2057–2072, <https://doi.org/10.5194/acp-20-2057-2020>, 2020.
- Atkinson, J. D., Murray, B. J., Woodhouse, M. T., Whale, T. F., Baustian, K. J., Carslaw, K. S., Dobbie, S., O'Sullivan, D., and Malkin, T. L.: The importance of feldspar for ice nucleation by mineral dust in mixed-phase clouds, *Nature*, 498, 355–358, <https://doi.org/10.1038/nature12278>, 2013.
- Avzianova, E. and Brooks, S. D.: Raman spectroscopy of glyoxal oligomers in aqueous solutions, *Spectrochimica Acta Part A: Molecular and Biomolecular Spectroscopy*, 101, 40–48, <https://doi.org/10.1016/j.saa.2012.09.050>, 2013.
- Baldo, C., Formenti, P., Di Biagio, C., Lu, G., Song, C., Cazaunau, M., Pangui, E., Doussin, J.-F., Dagsson-Waldhauserova, P., Arnalds, O., Beddows, D., MacKenzie, A. R., and Shi, Z.: Complex refractive index and single scattering albedo of Icelandic dust in the shortwave part of the spectrum, *Atmos. Chem. Phys.*, 23, 7975–8000, <https://doi.org/10.5194/acp-23-7975-2023>, 2023.
- Battaglia, F., Baldo, C., Cazaunau, M., Bergé, A., Pangui, E., Picquet-Varrault, B., Doussin, J.-F., and Formenti, P.: Protocol for generating realistic submicron mono-dispersed mineral dust particles in simulation chambers and laboratory experiments, *Aerosol Science and Technology*, 59, 357–369, <https://doi.org/10.1080/02786826.2024.2442518>, 2025.
- Bauer, S. E., Mishchenko, M. I., Lacis, A. A., Zhang, S., Perlwitz, J., and Metzger, S. M.: Do sulfate and nitrate coatings on mineral dust have important effects on radiative properties and climate modeling?, *J. Geophys. Res.*, 112, D06307, <https://doi.org/10.1029/2005JD006977>, 2007.
- Brégonzio-Rozier, L., Giorio, C., Siekmann, F., Pangui, E., Morales, S. B., Temime-Roussel, B., Gratien, A., Michoud, V., Cazaunau, M., DeWitt, H. L., Tapparo, A., Monod, A., and Doussin, J.-F.: Secondary organic aerosol formation from isoprene photooxidation during cloud condensation–evaporation cycles, *Atmos. Chem. Phys.*, 16, 1747–1760, <https://doi.org/10.5194/acp-16-1747-2016>, 2016.
- Buxton, G. V., Malone, T. N., and Arthur Salmon, G.: Oxidation of glyoxal initiated by OH in oxygenated aqueous solution, *Faraday Trans.*, 93, 2889–2891, <https://doi.org/10.1039/a701468f>, 1997.
- Carlton, A. G., Turpin, B. J., Altieri, K. E., Seitzinger, S., Reff, A., Lim, H.-J., and Ervens, B.: Atmospheric oxalic acid and SOA production from glyoxal: Results of aqueous photooxidation experiments, *Atmospheric Environment*, 41, 7588–7602, <https://doi.org/10.1016/j.atmosenv.2007.05.035>, 2007.
- Castellanos, P., Colarco, P., Espinosa, W. R., Guzewich, S. D., Levy, R. C., Miller, R. L., Chin, M., Kahn, R. A., Kemppinen, O., Moosmüller, H., Nowotnick, E. P., Rocha-Lima, A., Smith, M. D., Yorks, J. E., and Yu, H.: Mineral dust optical properties for remote sensing and global modeling: A review, *Remote Sensing of Environment*, 303, 113982, <https://doi.org/10.1016/j.rse.2023.113982>, 2024.
- Chan, C., Jacob, D. J., Marais, E. A., Yu, K., Travis, K. R., Kim, P. S., Fisher, J. A., Zhu, L., Wolfe, G. M., Hanisco, T. F., Keutsch, F. N., Kaiser, J., Min, K.-E., Brown, S. S., Washenfelder, R. A.,

941 González Abad, G., and Chance, K.: Glyoxal yield from isoprene oxidation and relation to
 942 formaldehyde: chemical mechanism, constraints from SENEX aircraft observations, and
 943 interpretation of OMI satellite data, *Atmos. Chem. Phys.*, 17, 8725–8738,
 944 <https://doi.org/10.5194/acp-17-8725-2017>, 2017.

945 Chen, S., Chen, J., Zhang, Y., Lin, J., Bi, H., Song, H., Chen, Y., Lian, L., Liu, C., and Zhang, R.:
 946 Anthropogenic dust: sources, characteristics and emissions, *Environ. Res. Lett.*, 18, 103002,
 947 <https://doi.org/10.1088/1748-9326/acf479>, 2023.

948 Chirizzi, D.: Influence of Saharan dust outbreaks and carbon content on oxidative potential of water-
 949 soluble fractions of PM_{2.5} and PM₁₀, *Atmospheric Environment*, 2017.

950 Crowley, J. N., Ammann, M., Cox, R. A., Hynes, R. G., Jenkin, M. E., Mellouki, A., Rossi, M. J., Troe,
 951 J., and Wallington, T. J.: Evaluated kinetic and photochemical data for atmospheric chemistry:
 952 Volume V – heterogeneous reactions on solid substrates, *Atmos. Chem. Phys.*, 10, 9059–9223,
 953 <https://doi.org/10.5194/acp-10-9059-2010>, 2010.

954 De Haan, D. O., Hawkins, L. N., Jansen, K., Welsh, H. G., Pednekar, R., De Loera, A., Jimenez, N. G.,
 955 Tolbert, M. A., Cazaunau, M., Gratien, A., Bergé, A., Pangui, E., Formenti, P., and Doussin, J.-
 956 F.: Glyoxal's impact on dry ammonium salts: fast and reversible surface aerosol browning, *Atmos.*
 957 *Chem. Phys.*, 20, 9581–9590, <https://doi.org/10.5194/acp-20-9581-2020>, 2020.

958 De Haan, D. O., Hawkins, L. N., Wickremasinghe, P. D., Andretta, A. D., Dignum, J. R., De Haan, A. C.,
 959 Welsh, H. G., Pennington, E. A., Cui, T., Surratt, J. D., Cazaunau, M., Pangui, E., and Doussin,
 960 J.-F.: Brown Carbon from Photo-Oxidation of Glyoxal and SO₂ in Aqueous Aerosol, *ACS Earth*
 961 *Space Chem.*, 7, 1131–1140, <https://doi.org/10.1021/acsearthspacechem.3c00035>, 2023.

962 Denjean, C., Formenti, P., Picquet-Varrault, B., Katrib, Y., Pangui, E., Zapf, P., and Doussin, J. F.: A
 963 new experimental approach to study the hygroscopic and optical properties of aerosols:
 964 application to ammonium sulfate particles, *Atmos. Meas. Tech.*, 7, 183–197,
 965 <https://doi.org/10.5194/amt-7-183-2014>, 2014.

966 Di Biagio, C., Formenti, P., Balkanski, Y., Caponi, L., Cazaunau, M., Pangui, E., Journet, E., Nowak, S.,
 967 Caquineau, S., Andreae, M. O., Kandler, K., Saeed, T., Piketh, S., Seibert, D., Williams, E., and
 968 Doussin, J.-F.: Global scale variability of the mineral dust long-wave refractive index: a new
 969 dataset of in situ measurements for climate modeling and remote sensing, *Atmos. Chem. Phys.*,
 970 17, 1901–1929, <https://doi.org/10.5194/acp-17-1901-2017>, 2017.

971 Di Biagio, C., Formenti, P., Balkanski, Y., Caponi, L., Cazaunau, M., Pangui, E., Journet, E., Nowak, S.,
 972 Andreae, M. O., Kandler, K., Saeed, T., Piketh, S., Seibert, D., Williams, E., and Doussin, J.-F.:
 973 Complex refractive indices and single-scattering albedo of global dust aerosols in the shortwave
 974 spectrum and relationship to size and iron content, *Atmos. Chem. Phys.*, 19, 15503–15531,
 975 <https://doi.org/10.5194/acp-19-15503-2019>, 2019.

976 Dupart, Y., King, S. M., Nekat, B., Nowak, A., Wiedensohler, A., Herrmann, H., David, G., Thomas, B.,
 977 Miffre, A., Rairoux, P., D'Anna, B., and George, C.: Mineral dust photochemistry induces
 978 nucleation events in the presence of SO₂, *Proc. Natl. Acad. Sci. U.S.A.*, 109, 20842–20847,
 979 <https://doi.org/10.1073/pnas.1212297109>, 2012.

980 Ervens, B. and Volkamer, R.: Glyoxal processing by aerosol multiphase chemistry: towards a kinetic
 981 modeling framework of secondary organic aerosol formation in aqueous particles, *Atmos. Chem.*
 982 *Phys.*, 10, 8219–8244, <https://doi.org/10.5194/acp-10-8219-2010>, 2010.

983 Fröhlich, R., Cubison, M. J., Slowik, J. G., Bukowiecki, N., Prévôt, A. S. H., Baltensperger, U., Schneider,
 984 J., Kimmel, J. R., Gonin, M., Rohner, U., Worsnop, D. R., and Jayne, J. T.: The ToF-ACSM: a
 985 portable aerosol chemical speciation monitor with TOFMS detection, *Atmos. Meas. Tech.*, 6,
 986 3225–3241, <https://doi.org/10.5194/amt-6-3225-2013>, 2013.

987 Fu, T.-M., Jacob, D. J., Wittrock, F., Burrows, J. P., Vrekoussis, M., and Henze, D. K.: Global budgets
 988 of atmospheric glyoxal and methylglyoxal, and implications for formation of secondary organic
 989 aerosols, *J. Geophys. Res.*, 113, D15303, <https://doi.org/10.1029/2007JD009505>, 2008.

990 Galloway, M. M., Chhabra, P. S., Chan, A. W. H., Surratt, J. D., Flagan, R. C., Seinfeld, J. H., and
 991 Keutsch, F. N.: Glyoxal uptake on ammonium sulphate seed aerosol: reaction products and
 992 reversibility of uptake under dark and irradiated conditions, *Atmos. Chem. Phys.*, 2009.

993 Giorio, C., Monod, A., Brégonzio-Rozier, L., DeWitt, H. L., Cazaunau, M., Temime-Roussel, B., Gratien,
 994 A., Michoud, V., Pangui, E., Ravier, S., Zielinski, A. T., Tapparo, A., Vermeylen, R., Claeys, M.,
 995 Voisin, D., Kalberer, M., and Doussin, J.-F.: Cloud Processing of Secondary Organic Aerosol from
 996 Isoprene and Methacrolein Photooxidation, *J. Phys. Chem. A*, 121, 7641–7654,
 997 <https://doi.org/10.1021/acs.jpca.7b05933>, 2017.

998 Giorio, C., D'Aronco, S., Di Marco, V., Badocco, D., Battaglia, F., Soldà, L., Pastore, P., and Tapparo,
 999 A.: Emerging investigator series: aqueous-phase processing of atmospheric aerosol influences
 1000 dissolution kinetics of metal ions in an urban background site in the Po Valley, *Environ. Sci.:
 1001 Processes Impacts*, 24, 884–897, <https://doi.org/10.1039/D2EM00023G>, 2022.

1002 Gomez, M. E., Lin, Y., Guo, S., & Zhang, R. (2015). Heterogeneous Chemistry of Glyoxal on Acidic
 1003 Solutions. An Oligomerization Pathway for Secondary Organic Aerosol Formation. *The Journal of
 1004 Physical Chemistry A*, 119(19), 4457–4463. <https://doi.org/10.1021/jp509916r>

1005 Goodman, A. L., Underwood, G. M., and Grassian, V. H.: Heterogeneous Reaction of NO₂:
 1006 Characterization of Gas-Phase and Adsorbed Products from the Reaction, 2NO₂(g) + H₂O(a)
 1007 → HONO(g) + HNO₃(a) on Hydrated Silica Particles, *J. Phys. Chem. A*, 103, 7217–7223,
 1008 <https://doi.org/10.1021/jp9910688>, 1999.

1009 Guo, Y., Wang, S., Zhu, J., Zhang, R., Gao, S., Saiz-Lopez, A., and Zhou, B.: Atmospheric
 1010 formaldehyde, glyoxal and their relations to ozone pollution under low- and high-NO_x regimes in
 1011 summertime Shanghai, China, *Atmospheric Research*, 258, 105635,
 1012 <https://doi.org/10.1016/j.atmosres.2021.105635>, 2021.

1013 Harrison, S. P., Kohfeld, K. E., Roelandt, C., and Claquin, T.: The role of dust in climate changes today,
 1014 at the last glacial maximum and in the future, *Earth-Science Reviews*, 54, 43–80,
 1015 [https://doi.org/10.1016/S0012-8252\(01\)00041-1](https://doi.org/10.1016/S0012-8252(01)00041-1), 2001.

1016 Hastings, W. P., Koehler, C. A., Bailey, E. L., & De Haan, D. O. (2005). Secondary Organic Aerosol
 1017 Formation by Glyoxal Hydration and Oligomer Formation: Humidity Effects and Equilibrium Shifts
 1018 during Analysis. *Environmental Science & Technology*, 39(22), 8728–8735.
 1019 <https://doi.org/10.1021/es050446l>

1020 Hettiarachchi, E. and Grassian, V. H.: Heterogeneous Reactions of Phenol on Different Components of
 1021 Mineral Dust Aerosol: Formation of Oxidized Organic and Nitro-Phenolic Compounds, *ACS EST
 1022 Air*, 1, 259–272, <https://doi.org/10.1021/acsestair.3c00042>, 2024.

1023 Horowitz, A., Meller, R., and Moortgat, G. K.: The UV–VIS absorption cross sections of the α-dicarbonyl
 1024 compounds: pyruvic acid, biacetyl and glyoxal, 2001.

1025 Hu, J., Chen, Z., Qin, X., and Dong, P.: Reversible and irreversible gas–particle partitioning of dicarbonyl
 1026 compounds observed in the real atmosphere, *Atmos. Chem. Phys.*, 22, 6971–6987,
 1027 <https://doi.org/10.5194/acp-22-6971-2022>, 2022.

1028 Joshi, N., Romanias, M. N., Riffault, V., and Thevenet, F.: Investigating water adsorption onto natural
 1029 mineral dust particles: Linking DRIFTS experiments and BET theory, *Aeolian Research*, 27, 35–
 1030 45, <https://doi.org/10.1016/j.aeolia.2017.06.001>, 2017.

1031 Lai, A. C. and Nazaroff, W. W.: MODELING INDOOR PARTICLE DEPOSITION FROM TURBULENT
 1032 FLOW ONTO SMOOTH SURFACES, *Journal of Aerosol Science*, 31, 463–476,
 1033 [https://doi.org/10.1016/S0021-8502\(99\)00536-4](https://doi.org/10.1016/S0021-8502(99)00536-4), 2000.

1034 Kalberer, M., Paulsen, D., Sax, M., Steinbacher, M., Dommen, J., Prevot, A. S. H., Fisseha, R.,
 1035 Weingartner, E., Frankevich, V., Zenobi, R., and Baltensperger, U.: Identification of Polymers as
 1036 Major Components of Atmospheric Organic Aerosols, *Science*, 303, 1659–1662,
 1037 <https://doi.org/10.1126/science.1092185>, 2004.

1038 Kluge, F., Hüneke, T., Lerot, C., Rosanka, S., Rotermund, M. K., Taraborrelli, D., Weyland, B., and
 1039 Pfeilsticker, K.: Airborne glyoxal measurements in the marine and continental atmosphere:

1040 comparison with TROPOMI observations and EMAC simulations, *Atmos. Chem. Phys.*, 23, 1369–
1041 1401, <https://doi.org/10.5194/acp-23-1369-2023>, 2023.

1042 Knippertz, P. and Stuut, J.-B. W. (Eds.): *Mineral Dust: A Key Player in the Earth System*, Springer
1043 Netherlands, Dordrecht, <https://doi.org/10.1007/978-94-017-8978-3>, 2014.

1044 Knote, C., Hodzic, A., Jimenez, J. L., Volkamer, R., Orlando, J. J., Baidar, S., Brioude, J., Fast, J.,
1045 Gentner, D. R., Goldstein, A. H., Hayes, P. L., Knighton, W. B., Oetjen, H., Setyan, A., Stark, H.,
1046 Thalman, R., Tyndall, G., Washenfelder, R., Waxman, E., and Zhang, Q.: Simulation of semi-
1047 explicit mechanisms of SOA formation from glyoxal in aerosol in a 3-D model, *Atmos. Chem.*
1048 *Phys.*, 14, 6213–6239, <https://doi.org/10.5194/acp-14-6213-2014>, 2014.

1049 Kok, J. F., Adebisi, A. A., Albani, S., Balkanski, Y., Checa-Garcia, R., Chin, M., Colarco, P. R., Hamilton,
1050 D. S., Huang, Y., Ito, A., Klose, M., Li, L., Mahowald, N. M., Miller, R. L., Obiso, V., Pérez García-
1051 Pando, C., Rocha-Lima, A., and Wan, J. S.: Contribution of the world's main dust source regions
1052 to the global cycle of desert dust, *Aerosols/Atmospheric Modelling/Troposphere/Physics (physical*
1053 *properties and processes)*, <https://doi.org/10.5194/acp-2021-4>, 2021.

1054 Kok, J. F., Storelvmo, T., Karydis, V. A., Adebisi, A. A., Mahowald, N. M., Evan, A. T., He, C., and Leung,
1055 D. M.: Mineral dust aerosol impacts on global climate and climate change, *Nat Rev Earth Environ*,
1056 4, 71–86, <https://doi.org/10.1038/s43017-022-00379-5>, 2023.

1057 Kourtchev, I., Doussin, J.-F., Giorio, C., Mahon, B., Wilson, E. M., Maurin, N., Pangu, E., Venables, D.
1058 S., Wenger, J. C., and Kalberer, M.: Molecular composition of fresh and aged secondary organic
1059 aerosol from a mixture of biogenic volatile compounds: a high-resolution mass spectrometry
1060 study, *Atmos. Chem. Phys.*, 15, 5683–5695, <https://doi.org/10.5194/acp-15-5683-2015>, 2015.

1061 Kroll, J. H., Ng, N. L., Murphy, S. M., Varutbangkul, V., Flagan, R. C., and Seinfeld, J. H.: Chamber
1062 studies of secondary organic aerosol growth by reactive uptake of simple carbonyl compounds,
1063 *J. Geophys. Res.*, 110, 2005JD006004, <https://doi.org/10.1029/2005JD006004>, 2005.

1064 Kua, J., Hanley, S. W., & De Haan, D. O. (2008). Thermodynamics and Kinetics of Glyoxal Dimer
1065 Formation: A Computational Study. *The Journal of Physical Chemistry A*, 112(1), 66–72.
1066 <https://doi.org/10.1021/jp076573g>

1067 Lewis, A. C., Hopkins, J. R., Carslaw, D. C., Hamilton, J. F., Nelson, B. S., Stewart, G., Dornie, J.,
1068 Passant, N., and Murrells, T.: An increasing role for solvent emissions and implications for future
1069 measurements of volatile organic compounds, *Phil. Trans. R. Soc. A.*, 378, 20190328,
1070 <https://doi.org/10.1098/rsta.2019.0328>, 2020.

1071 Li, G., Cheng, Y., Kuhn, U., Xu, R., Yang, Y., Meusel, H., Wang, Z., Ma, N., Wu, Y., Li, M., Williams, J.,
1072 Hoffmann, T., Ammann, M., Pöschl, U., Shao, M., and Su, H.: Physicochemical uptake and
1073 release of volatile organic compounds by soil in coated-wall flow tube experiments with ambient
1074 air, *Atmos. Chem. Phys.*, 19, 2209–2232, <https://doi.org/10.5194/acp-19-2209-2019>, 2019.

1075 Li, L., Mahowald, N. M., Miller, R. L., Pérez García-Pando, C., Klose, M., Hamilton, D. S., Gonçalves
1076 Ageitos, M., Ginoux, P., Balkanski, Y., Green, R. O., Kalashnikova, O., Kok, J. F., Obiso, V.,
1077 Paynter, D., and Thompson, D. R.: Quantifying the range of the dust direct radiative effect due to
1078 source mineralogy uncertainty, *Atmos. Chem. Phys.*, 21, 3973–4005, <https://doi.org/10.5194/acp-21-3973-2021>, 2021.

1080 Li, Q., Gong, D., Wang, H., Wang, Y., Han, S., Wu, G., Deng, S., Yu, P., Wang, W., and Wang, B.: Rapid
1081 increase in atmospheric glyoxal and methylglyoxal concentrations in Lhasa, Tibetan Plateau:
1082 Potential sources and implications, *Science of The Total Environment*, 824, 153782,
1083 <https://doi.org/10.1016/j.scitotenv.2022.153782>, 2022.

1084 Liggio, J.: Reactive uptake of glyoxal by particulate matter, *J. Geophys. Res.*, 110, D10304,
1085 <https://doi.org/10.1029/2004JD005113>, 2005a.

1086 Liggio, J., Li, S.-M., and McLaren, R.: Heterogeneous Reactions of Glyoxal on Particulate Matter:
1087 Identification of Acetals and Sulfate Esters, *Environ. Sci. Technol.*, 39, 1532–1541,
1088 <https://doi.org/10.1021/es048375y>, 2005b.

- 1089 Lim, Y. B., Tan, Y., Perri, M. J., Seitzinger, S. P., and Turpin, B. J.: Aqueous chemistry and its role in
1090 secondary organic aerosol (SOA) formation, *Atmos. Chem. Phys.*, 10, 10521–10539,
1091 <https://doi.org/10.5194/acp-10-10521-2010>, 2010.
- 1092 Ling, Z., Xie, Q., Shao, M., Wang, Z., Wang, T., Guo, H., and Wang, X.: Formation and sink of glyoxal
1093 and methylglyoxal in a polluted subtropical environment: observation-based photochemical
1094 analysis and impact evaluation, *Atmos. Chem. Phys.*, 20, 11451–11467,
1095 <https://doi.org/10.5194/acp-20-11451-2020>, 2020.
- 1096 Liu, C., Chu, B., Liu, Y., Ma, Q., Ma, J., He, H., Li, J., and Hao, J.: Effect of mineral dust on secondary
1097 organic aerosol yield and aerosol size in α -pinene/NO_x photo-oxidation, *Atmospheric*
1098 *Environment*, 77, 781–789, <https://doi.org/10.1016/j.atmosenv.2013.05.064>, 2013.
- 1099 Loeffler, K. W., Koehler, C. A., Paul, N. M., & De Haan, D. O. (2006). Oligomer Formation in Evaporating
1100 Aqueous Glyoxal and Methyl Glyoxal Solutions. *Environmental Science & Technology*, 40(20),
1101 6318–6323. <https://doi.org/10.1021/es060810w>
- 1102 Mahowald, N., Albani, S., Kok, J. F., Engelstaeder, S., Scanza, R., Ward, D. S., and Flanner, M. G.: The
1103 size distribution of desert dust aerosols and its impact on the Earth system, *Aeolian Research*,
1104 15, 53–71, <https://doi.org/10.1016/j.aeolia.2013.09.002>, 2014.
- 1105 Ng, N. L., Canagaratna, M. R., Jimenez, J. L., Chhabra, P. S., Seinfeld, J. H., and Worsnop, D. R.:
1106 Changes in organic aerosol composition with aging inferred from aerosol mass spectra, *Atmos.*
1107 *Chem. Phys.*, 11, 6465–6474, <https://doi.org/10.5194/acp-11-6465-2011>, 2011.
- 1108 Nie, W., Ding, A., Wang, T., Kerminen, V.-M., George, C., Xue, L., Wang, W., Zhang, Q., Petäjä, T., Qi,
1109 X., Gao, X., Wang, X., Yang, X., Fu, C., and Kulmala, M.: Polluted dust promotes new particle
1110 formation and growth, *Sci Rep*, 4, 6634, <https://doi.org/10.1038/srep06634>, 2014.
- 1111 Nieder, R., Benbi, D. K., and Reichl, F. X.: Soil-Borne Particles and Their Impact on Environment and
1112 Human Health, in: *Soil Components and Human Health*, Springer Netherlands, Dordrecht, 99–
1113 177, https://doi.org/10.1007/978-94-024-1222-2_3, 2018.
- 1114 Nozière, B., Dziedzic, P., and Córdova, A.: Products and Kinetics of the Liquid-Phase Reaction of
1115 Glyoxal Catalyzed by Ammonium Ions (NH₄⁺), *J. Phys. Chem. A*, 113, 231–237,
1116 <https://doi.org/10.1021/jp8078293>, 2009.
- 1117 Ooki, A. and Uematsu, M.: Chemical interactions between mineral dust particles and acid gases during
1118 Asian dust events, *J. Geophys. Res.*, 110, 2004JD004737,
1119 <https://doi.org/10.1029/2004JD004737>, 2005.
- 1120 Ortiz-Montalvo, D. L., Häkkinen, S. A. K., Schwier, A. N., Lim, Y. B., McNeill, V. F., and Turpin, B. J.:
1121 Ammonium Addition (and Aerosol pH) Has a Dramatic Impact on the Volatility and Yield of Glyoxal
1122 Secondary Organic Aerosol, *Environ. Sci. Technol.*, 48, 255–262,
1123 <https://doi.org/10.1021/es4035667>, 2014.
- 1124 Ponczek, M., Hayeck, N., Emmelin, C., and George, C.: Heterogeneous photochemistry of dicarboxylic
1125 acids on mineral dust, *Atmospheric Environment*, 212, 262–271,
1126 <https://doi.org/10.1016/j.atmosenv.2019.05.032>, 2019.
- 1127 Romanias, M. N., El Zein, A., and Bedjanian, Y.: Heterogeneous Interaction of H₂O₂ with TiO₂
1128 Surface under Dark and UV Light Irradiation Conditions, *J. Phys. Chem. A*, 116, 8191–8200,
1129 <https://doi.org/10.1021/jp305366v>, 2012.
- 1130 Romanías, Manolis N., Habib Ourrad, Frédéric Thévenet, and Véronique Riffault. 2016. "Investigating
1131 the Heterogeneous Interaction of VOCs with Natural Atmospheric Particles: Adsorption of
1132 Limonene and Toluene on Saharan Mineral Dusts." *The Journal of Physical Chemistry A*
1133 120(8):1197–1212. doi: 10.1021/acs.jpca.5b10323.
- 1134 Rossignol, S., Aregahegn, K. Z., Tinel, L., Fine, L., Nozière, B., and George, C.: Glyoxal Induced
1135 Atmospheric Photosensitized Chemistry Leading to Organic Aerosol Growth, *Environ. Sci.*
1136 *Technol.*, 48, 3218–3227, <https://doi.org/10.1021/es405581g>, 2014.
- 1137 Rubasinghege, G., Ogden, S., Baltrusaitis, J., and Grassian, V. H.: Heterogeneous Uptake and
1138 Adsorption of Gas-Phase Formic Acid on Oxide and Clay Particle Surfaces: The Roles of Surface

Hydroxyl Groups and Adsorbed Water in Formic Acid Adsorption and the Impact of Formic Acid Adsorption on Water Uptake, *J. Phys. Chem. A*, 117, 11316–11327, <https://doi.org/10.1021/jp408169w>, 2013.

Safi Shalamzari, M., Ryabtsova, O., Kahnt, A., Vermeylen, R., Hérent, M., Quetin-Leclercq, J., Van Der Veken, P., Maenhaut, W., and Claeys, M.: Mass spectrometric characterization of organosulfates related to secondary organic aerosol from isoprene, *Rapid Comm Mass Spectrometry*, 27, 784–794, <https://doi.org/10.1002/rcm.6511>, 2013.

Schwier, A. N., Sareen, N., Mitroo, D., Shapiro, E. L., and McNeill, V. F.: Glyoxal-Methylglyoxal Cross-Reactions in Secondary Organic Aerosol Formation, *Environ. Sci. Technol.*, 44, 6174–6182, <https://doi.org/10.1021/es101225q>, 2010.

Seisel, S., Lian, Y., Keil, T., Trukhin, M. E., and Zellner, R.: Kinetics of the interaction of water vapour with mineral dust and soot surfaces at $T = 298$ K, *Phys. Chem. Chem. Phys.*, 6, 1926–1932, <https://doi.org/10.1039/B314568A>, 2004.

Shapiro, E. L., Szprengiel, J., Sareen, N., Jen, C. N., Giordano, M. R., and McNeill, V. F.: Light-absorbing secondary organic material formed by glyoxal in aqueous aerosol mimics, *Atmos. Chem. Phys.*, 2009.

Shen, X., Wu, H., Zhao, Y., Huang, D., Huang, L., and Chen, Z.: Heterogeneous reactions of glyoxal on mineral particles: A new avenue for oligomers and organosulfate formation, *Atmospheric Environment*, 131, 133–140, <https://doi.org/10.1016/j.atmosenv.2016.01.048>, 2016.

Shrivastava, M., Cappa, C. D., Fan, J., Goldstein, A. H., Guenther, A. B., Jimenez, J. L., Kuang, C., Laskin, A., Martin, S. T., Ng, N. L., Petaja, T., Pierce, J. R., Rasch, P. J., Roldin, P., Seinfeld, J. H., Shilling, J., Smith, J. N., Thornton, J. A., Volkamer, R., Wang, J., Worsnop, D. R., Zaveri, R. A., Zelenyuk, A., and Zhang, Q.: Recent advances in understanding secondary organic aerosol: Implications for global climate forcing, *Reviews of Geophysics*, 55, 509–559, <https://doi.org/10.1002/2016RG000540>, 2017.

Song, Q. and Osada, K.: Direct measurement of aerosol acidity using pH testing paper and hygroscopic equilibrium under high relative humidity, *Atmospheric Environment*, 261, 118605, <https://doi.org/10.1016/j.atmosenv.2021.118605>, 2021.

Steinke, I., Funk, R., Busse, J., Iturri, A., Kirchen, S., Leue, M., Möhler, O., Schwartz, T., Schnaiter, M., Sierau, B., Toprak, E., Ullrich, R., Ulrich, A., Hoose, C., and Leisner, T.: Ice nucleation activity of agricultural soil dust aerosols from Mongolia, Argentina, and Germany, *JGR Atmospheres*, 121, <https://doi.org/10.1002/2016JD025160>, 2016.

Sun, Y. L., Zhang, Q., Anastasio, C., and Sun, J.: Insights into secondary organic aerosol formed via aqueous-phase reactions of phenolic compounds based on high resolution mass spectrometry, *Atmos. Chem. Phys.*, 10, 4809–4822, <https://doi.org/10.5194/acp-10-4809-2010>, 2010.

Tang, M., Huang, X., Lu, K., Ge, M., Li, Y., Cheng, P., Zhu, T., Ding, A., Zhang, Y., Gligorovski, S., Song, W., Ding, X., Bi, X., and Wang, X.: Heterogeneous reactions of mineral dust aerosol: implications for tropospheric oxidation capacity, *Atmos. Chem. Phys.*, 17, 11727–11777, <https://doi.org/10.5194/acp-17-11727-2017>, 2017.

Tegen, I. and Fung, I.: Contribution to the atmospheric mineral aerosol load from land surface modification, *J. Geophys. Res.*, 100, 18707, <https://doi.org/10.1029/95JD02051>, 1995.

Trainic, M., Abo Riziq, A., Lavi, A., Flores, J. M., and Rudich, Y.: The optical, physical and chemical properties of the products of glyoxal uptake on ammonium sulfate seed aerosols, *Atmos. Chem. Phys.*, 11, 9697–9707, <https://doi.org/10.5194/acp-11-9697-2011>, 2011.

Turpin, B. J. and Huntzicker, J. J.: Identification of secondary organic aerosol episodes and quantitation of primary and secondary organic aerosol concentrations during SCAQS, *Atmospheric Environment*, 29, 3527–3544, [https://doi.org/10.1016/1352-2310\(94\)00276-Q](https://doi.org/10.1016/1352-2310(94)00276-Q), 1995.

Usher, C. R., Michel, A. E., and Grassian, V. H.: Reactions on Mineral Dust, *Chem. Rev.*, 103, 4883–4940, <https://doi.org/10.1021/cr020657y>, 2003.

1188 Volkamer, R., Platt, U., and Wirtz, K.: Primary and Secondary Glyoxal Formation from Aromatics:
 1189 Experimental Evidence for the Bicycloalkyl-Radical Pathway from Benzene, Toluene, and p -
 1190 Xylene, *J. Phys. Chem. A*, 105, 7865–7874, <https://doi.org/10.1021/jp010152w>, 2001.

1191 Volkamer, R., Spietz, P., Burrows, J., and Platt, U.: High-resolution absorption cross-section of glyoxal
 1192 in the UV–vis and IR spectral ranges, *Journal of Photochemistry and Photobiology A: Chemistry*,
 1193 172, 35–46, <https://doi.org/10.1016/j.jphotochem.2004.11.011>, 2005.

1194 Volkamer, R., San Martini, F., Molina, L. T., Salcedo, D., Jimenez, J. L., and Molina, M. J.: A missing
 1195 sink for gas-phase glyoxal in Mexico City: Formation of secondary organic aerosol, *Geophysical*
 1196 *Research Letters*, 34, 2007GL030752, <https://doi.org/10.1029/2007GL030752>, 2007.

1197 Vrekoussis, M., Wittrock, F., Richter, A., Burrows, J. P., and Cho, C.: Temporal and spatial variability of
 1198 glyoxal as observed from space, *Atmos. Chem. Phys.*, 2009.

1199 Wagner, C., Hanisch, F., Holmes, N., de Coninck, H., Schuster, G., and Crowley, J. N.: The interaction
 1200 of N₂O₅ with mineral dust: aerosol flow tube and Knudsen reactor studies, *Atmos. Chem. Phys.*,
 1201 2008.

1202 Walker, H., Stone, D., Ingham, T., Hackenberg, S., Cryer, D., Punjabi, S., Read, K., Lee, J., Whalley,
 1203 L., Spracklen, D. V., Carpenter, L. J., Arnold, S. R., and Heard, D. E.: Observations and modelling
 1204 of glyoxal in the tropical Atlantic marine boundary layer, *Atmos. Chem. Phys.*, 22, 5535–5557,
 1205 <https://doi.org/10.5194/acp-22-5535-2022>, 2022.

1206 Wang, G., Cheng, C., Meng, J., Huang, Y., Li, J., and Ren, Y.: Field observation on secondary organic
 1207 aerosols during Asian dust storm periods: Formation mechanism of oxalic acid and related
 1208 compounds on dust surface, *Atmospheric Environment*, 113, 169–176,
 1209 <https://doi.org/10.1016/j.atmosenv.2015.05.013>, 2015.

1210 Wang, J., Doussin, J. F., Perrier, S., Perraudin, E., Katrib, Y., Pangui, E., and Picquet-Varrault, B.:
 1211 Design of a new multi-phase experimental simulation chamber for atmospheric photosmog,
 1212 aerosol and cloud chemistry research, *Atmos. Meas. Tech.*, 4, 2465–2494,
 1213 <https://doi.org/10.5194/amt-4-2465-2011>, 2011.

1214 Washenfelder, R. A., Young, C. J., Brown, S. S., Angevine, W. M., Atlas, E. L., Blake, D. R., Bon, D. M.,
 1215 Cubison, M. J., De Gouw, J. A., Dusanter, S., Flynn, J., Gilman, J. B., Graus, M., Griffith, S.,
 1216 Grossberg, N., Hayes, P. L., Jimenez, J. L., Kuster, W. C., Lefer, B. L., Pollack, I. B., Ryerson, T.
 1217 B., Stark, H., Stevens, P. S., and Trainer, M. K.: The glyoxal budget and its contribution to organic
 1218 aerosol for Los Angeles, California, during CalNex 2010: GLYOXAL BUDGET FOR LOS
 1219 ANGELES, *J. Geophys. Res.*, 116, <https://doi.org/10.1029/2011JD016314>, 2011.

1220 Webb, N. P. and Pierre, C.: Quantifying Anthropogenic Dust Emissions, *Earth's Future*, 6, 286–295,
 1221 <https://doi.org/10.1002/2017EF000766>, 2018.

1222 Xu, K., Liu, Y., Li, C., Zhang, C., Liu, X., Li, Q., Xiong, M., Zhang, Y., Yin, S., and Ding, Y.: Enhanced
 1223 secondary organic aerosol formation during dust episodes by photochemical reactions in the
 1224 winter in Wuhan, *Journal of Environmental Sciences*, 133, 70–82,
 1225 <https://doi.org/10.1016/j.jes.2022.04.018>, 2023.

1226 Zeineddine, M. N., Romanias, M. N., Gaudion, V., Riffault, V., and Thévenet, F.: Heterogeneous
 1227 Interaction of Isoprene with Natural Gobi Dust, *ACS Earth Space Chem.*, 1, 236–243,
 1228 <https://doi.org/10.1021/acsearthspacechem.7b00050>, 2017.

1229 Zeineddine, M. N., Urupina, D., Romanias, M. N., Riffault, V., and Thevenet, F.: Uptake and reactivity
 1230 of acetic acid on Gobi dust and mineral surrogates: A source of oxygenated volatile organic
 1231 compounds in the atmosphere?, *Atmospheric Environment*, 294, 119509,
 1232 <https://doi.org/10.1016/j.atmosenv.2022.119509>, 2023.

1233 Zhang, X., He, A., Guo, R., Zhao, Y., Yang, L., Morita, S., Xu, Y., Noda, I., and Ozaki, Y.: A new approach
 1234 to removing interference of moisture from FTIR spectrum, *Spectrochimica Acta Part A: Molecular*
 1235 *and Biomolecular Spectroscopy*, 265, 120373, <https://doi.org/10.1016/j.saa.2021.120373>, 2022.

1236 Zhang, Y., He, L., Sun, X., Ventura, O. N., & Herrmann, H. (2022). Theoretical Investigation on the
 1237 Oligomerization of Methylglyoxal and Glyoxal in Aqueous Atmospheric Aerosol Particles. *ACS*

1238 Earth and Space Chemistry, 6(4), 1031–1043.
1239 <https://doi.org/10.1021/acsearthspacechem.1c00422>

1240 Zielinski, A. T., Kourtchev, I., Bortolini, C., Fuller, S. J., Giorio, C., Popoola, O. A. M., Bogialli, S.,
1241 Tapparo, A., Jones, R. L., and Kalberer, M.: A new processing scheme for ultra-high resolution
1242 direct infusion mass spectrometry data, *Atmospheric Environment*, 178, 129–139,
1243 <https://doi.org/10.1016/j.atmosenv.2018.01.034>, 2018.

1244

1245